

# Electromagnetics and Antenna Technology, Chapters 4 and 5

Alan J. Fenn

Senior Staff Member  
Lincoln Laboratory  
Massachusetts Institute of Technology  
244 Wood Street  
Lexington, MA 02420

March 7, 2017

# 4

## Omnidirectional Antennas

### 4.1 Introduction

This chapter describes simulations and measurements of antennas that are omnidirectional in azimuth. Omnidirectional coverage is desired in applications where the desired signal direction is arbitrary. Omnidirectional coverage can be provided for vertical polarization with vertical monopole or dipole antennas which can typically have a cylindrical or conical shape. A monopole antenna with a cone shape is referred to as a monocone or conical monopole. Similarly, a dipole antenna with cone-shaped arms is referred to as a bicone or biconical antenna. Omnidirectional horizontally polarized coverage can be achieved with horizontal loops or slotted cylinder antennas. Section 4.2 describes vertically polarized cylindrical and conical monopole antennas. Section 4.3 describes a vertically polarized discone antenna. The turnstile crossed dipole was described as an omnidirectional antenna in Chapter 1 (Section 1.12.2), where the arms were aligned in a plane. Section 4.4 describes an omnidirectional monopole array designed for simultaneous transmit and receive application. Section 4.5 describes omnidirectional horizontally polarized loop and slotted cylinder antennas. Section 4.6 investigates the turnstile crossed-dipole antenna where the dipole arms are swept back to provide omnidirectional pattern coverage for horizontal and vertical polarization. Each of the antennas described in this chapter can be considered wideband depending on how the bandwidth is defined, either in terms of the radiation pattern or impedance match or both. For transmit applications both the radiation pattern and impedance match will be important. For some receive applications involving communications, only the radiation pattern gain will be of primary importance as long as the communications link closes.

## 4.2 Monopole Antennas

### 4.2.1 Background for Cylindrical and Conical Monopoles

In this section, two types of antennas are considered here, cylindrical monopoles and conical monopoles over a ground plane [1-22]. The contrast between a cylindrical monopole and a conical monopole is depicted in the photograph shown in Figure 4.1. In this photograph each monopole has been



**Figure 4.1** Photograph of cylindrical and conical monopole antennas.

electrically attached to the center pin of a type-N microwave connector. The conical monopole is shown with a closed-end plate, which is known from the literature to have little effect on the input impedance and radiation pattern. Both cylindrical and conical monopoles are useful as single transmitting and receiving antennas, and in phased arrays [21]. In Figure 4.2, a photograph of a cylindrical monopole mounted in an array of like elements on an aluminum ground plane is shown. The optical reflection of the vertical monopole element

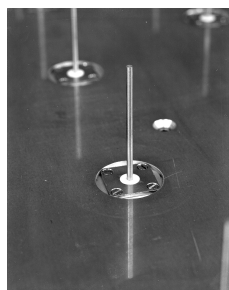


**Figure 4.2** Photograph of an array of cylindrical monopoles over a ground plane.

in the ground plane shows an optical image that appears the same as the electrical image due to the boundary conditions described in Chapter 1 (refer to Section 1.5 and Figure 1.31). The image of the monopole effectively forms an equivalent dipole in free space, which can be analyzed readily with

the method of moments. An equivalent dipole array example was shown previously in chapter 2 (see Figures 2.40 and 2.41). Alternately, the method of moments can be applied to the monopole and ground plane combination. A sketch of a cylindrical monopole over a conducting ground plane is shown in Figure 4.3. The base of the monopole is connected to a coaxial line that operates in the transverse electromagnetic (TEM) mode. Brown and

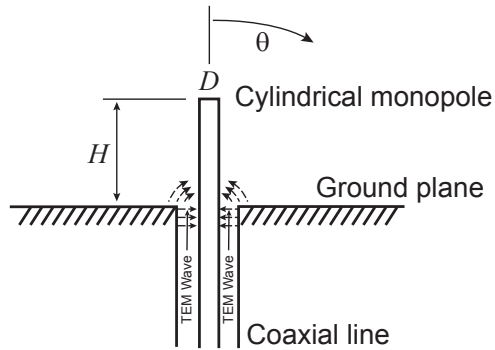


**Figure 4.3** Sketch of a cylindrical monopole over a ground plane, fed with a coaxial line.

Woodward have performed extensive measurements of the input impedance of cylindrical monopoles over a ground plane [22] as shown in Figures 4.4 (input resistance) and 4.5 (input reactance). These data were measured at

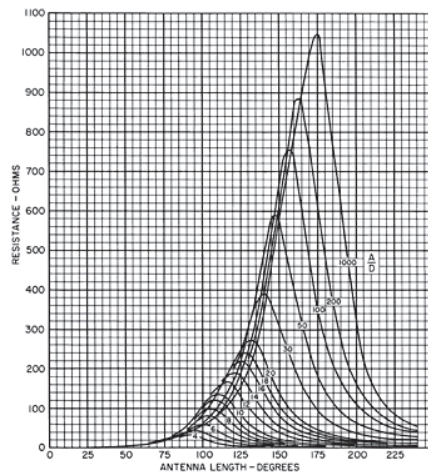


**Figure 4.4** Measured input resistance for a cylindrical monopole over a ground plane, fed with a coaxial line.



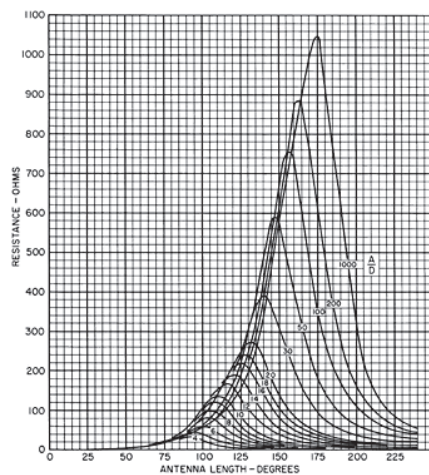


**Figure 4.5** Measured input reactance for a cylindrical monopole over a ground plane, fed with a coaxial line.

60 MHz with numerous physical size cylindrical monopoles with closed-end circular metal plate bases mounted over a circular metallic screen 3.66m in diameter and 6 wires per cm, which was placed on the earth's surface. A large variation in the input impedance of cylindrical monopoles occurs for thin-diameter cylinders where the length to diameter ratio is large. As the diameter of the cylindrical monopole increases for a fixed length, the input impedance tends to have a decreasing variation, which provides more bandwidth.

It should be noted that the input impedance of a monopole (either cylindrical or conical) is one half that of the equivalent dipole. The peak gain of a one-quarter wavelength cylindrical monopole over an infinite perfectly conducting ground plane is 5.1 dBi compared to the peak gain of a one-half wavelength dipole in free space which is 2.1 dBi. Referring to Figure 4.3, for an infinite perfectly conducting ground plane the monopole peak gain occurs at  $\theta = 90^\circ$ . When an infinite ground plane has a finite conductivity such as the earth's surface, the monopole radiated field is attenuated to a null in the far field at  $\theta = 90^\circ$ . For a monopole mounted on a finite ground plane, the beam peak is lifted up from  $\theta = 90^\circ$ . The monopole is omnidirectional with respect to the axis of the monopole.

Figure 4.6 shows a sketch of a conical monopole over a ground plane. The conical monopole is fed with a coaxial transmission line operating in the transverse electric mode (TEM). The cone is assumed to have vertical height  $H$ , slant length  $a$ , upper diameter  $D$ , and lower diameter  $d$ . The cone



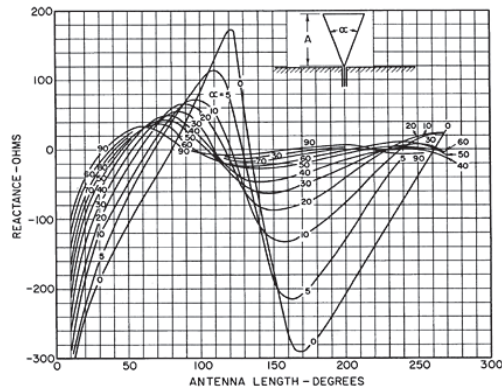


**Figure 4.8** Measured input reactance for a conical monopole over a ground plane, fed with a coaxial line.

ground plane 2.44m in diameter on the earth's surface. As the cone angle increases there is a decreased variation in the input impedance, which allows an increased bandwidth.

It is noted by Reich [6] that as the slant length (or height) of a conical monopole approaches one wavelength, the input impedance is approximately equal to the characteristic impedance. Referring to Figure 4.6 at the feed gap region, on transmit a TEM wave is launched (from the coaxial feed line) between the cone's base (apex) and ground plane, and the wave propagates outward until it reaches the antenna aperture represented by the the curved wavefront between points 1 and 2. At the edge discontinuity of the finite cone (point 1), a portion of the incident field will be scattered (diffracted) back towards the feed region and a portion will be transmitted (diffracted) into free space. When the wave reaches point 3 at the finite rim of the ground plane, a portion of the wave will be scattered (diffracted) back towards the feed and a portion will be transmitted (diffracted by the edge) into free space.

An approximate expression for the reflection coefficient of a finite monocone with slant length  $a$  on an infinite ground plane has been derived by Papas and King [10, 11]. The input impedance of a conical monopole can be determined by an eigenfunction expansion of the electric field components  $E_\theta$  and  $E_r$  and magnetic field component  $H_\phi$ . The tangential components are made continuous across the antenna aperture. Only the dominant mode of the coaxial feedline (transverse electric mode (TEM)) is included at the feed region. The approximate reflection coefficient  $\Gamma$  for cones with a large flare angle (cones with half-angle approximately  $30^\circ$  or larger) can be calculated for the TEM outgoing and TEM reflected wave at the fictitious

boundary surface at the cone aperture, as given by

$$\Gamma(ka) = e^{-2ika} \frac{1 + i \frac{60}{Z_o} \sum_{n=1}^{\infty} \frac{2n+1}{n(n+1)} [P_n(\cos \theta_o)]^2 \zeta_n(ka)}{-1 + i \frac{60}{Z_o} \sum_{n=1}^{\infty} \frac{2n+1}{n(n+1)} [P_n(\cos \theta_o)]^2 \zeta_n(ka)} \quad (4.3)$$

where  $i$  is the imaginary number,  $P_n(x)$  is the Legendre polynomial of order  $n$ ,  $k = 2\pi/\lambda$  is the wavenumber, and

$$\zeta(ka) = \frac{h_n^{(2)}(ka)}{h_{n-1}^{(2)}(ka) - \frac{n}{ka} h_n^{(2)}(ka)} \quad (4.4)$$

In Equation (4.3) the summation is performed over the odd integer values of  $n$ . In the zeta function defined by Equation (4.4),  $h_n^{(2)}(ka)$  is the spherical Hankel function of the second kind which is given by

$$h_n^{(2)}(ka) = j_n(ka) - i y_n(ka) \quad (4.5)$$

where  $j_n(ka)$  and  $y_n(ka)$  are the spherical Bessel functions of the first and second kind, respectively. The spherical Bessel functions of the first and second kind are computed from the Bessel functions of the first and second kind as,

$$j_n(ka) = \sqrt{\frac{\pi}{2ka}} J_{n+\frac{1}{2}}(ka) \quad (4.6)$$

$$y_n(ka) = \sqrt{\frac{\pi}{2ka}} Y_{n+\frac{1}{2}}(ka) \quad (4.7)$$

The conical monopole input impedance is then computed as

$$Z_{in} = Z_o \frac{1 + \Gamma}{1 - \Gamma} \quad (4.8)$$

where  $Z_o$  is the characteristic impedance of an infinite conical monopole over an infinite ground plane. Papas and King state that Equation (4.8) is valid when the cone flare angle is large and the characteristic impedance of the coaxial feed is equal to the characteristic impedance of the conical monopole.

The characteristic impedance of an infinite conical monopole over an infinite ground plane is given by the following equation [2, p. 105]

$$Z_o = \frac{1}{2} \sqrt{\frac{\mu}{\epsilon}} \frac{1}{\pi} \ln \cot \frac{\theta_o}{2} = \frac{1}{2} \eta \frac{1}{\pi} \ln \cot \frac{\theta_o}{2} \quad (4.9)$$

and in the free space case with  $\eta = \eta_o = 120\pi$

$$Z_o = 60 \ln \cot \frac{\theta_o}{2} \quad (4.10)$$

Using Equation (4.10) the characteristic impedance of an infinite monocone versus cone half angle on an infinite ground plane is shown in Figure 4-9.

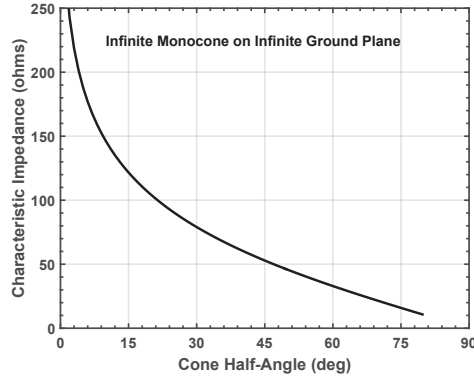


**Figure 4.9** Calculated characteristic impedance for an infinite conical monopole over an infinite ground plane.

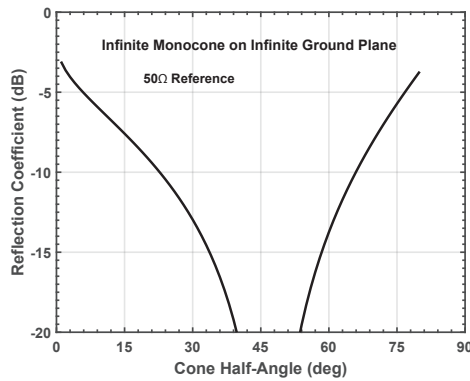


**Figure 4.10** Calculated reflection coefficient from the calculated characteristic impedance for an infinite conical monopole over a ground plane.

For example, when the infinite monocone has a half angle equal to  $45^\circ$ , the characteristic impedance is 52.9 ohms. A perfect impedance match to 50 ohms will occur for an infinite cone half angle equal to  $47^\circ$ . Figure 4.10 shows the calculated reflection coefficient for the infinite cone assuming a 50-ohm

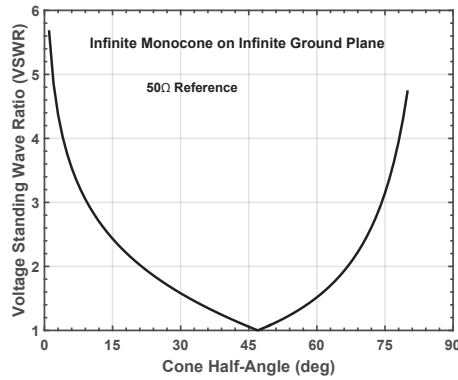


**Figure 4.11** Calculated VSWR from the calculated characteristic impedance for an infinite conical monopole over a ground plane.

coaxial transmission line is connected to the antenna, and Figure 4.11 shows the corresponding VSWR. According to Figure 4.11, the infinite cone will have a  $VSWR \leq 2.5$  for cone half-angles in the range of about  $15^\circ$  to  $70^\circ$ . For a given coaxial transmission line with a typical characteristic impedance of 50 ohms, a simplified design approach just uses the characteristic impedance of an infinite conical monopole to approximate the cone input impedance for finite cones that have a height one wavelength or longer.

The above discussions provide a theoretical approach to approximating the input impedance of conical monopoles. However, in this chapter, the preferred method for quantifying the input impedance, reflection coefficient, VSWR, mismatch loss, and radiation patterns is by the method of moments that performs a full-wave solution of the dielectric-loaded coaxial feed, finite cone and finite ground plane. The method of moments simulations can be used to adjust the conical monopole parameters to tune the antenna over a desired frequency band.

#### 4.2.2 An Example Ultrawideband Array Application With Monocone Antennas

Ultrawideband (UWB) communications antennas typically must transmit and receive ultrawideband waveforms without introducing significant amplitude and phase distortion. In many applications, it is desirable to have an array of antennas where each of the antennas has an omnidirectional radiation pattern characteristic. An antenna array allows the use of signal processing algorithms for adaptive nulling and direction finding. As is known from the literature, conical monopoles over a ground plane provide a suitable omnidirectional

antenna element for very wide bandwidth communications links [23–26]. As depicted in Figure 4.12, a sparse array of conical monopoles has been used in direction finding measurements as reported by Keller [23]. Other

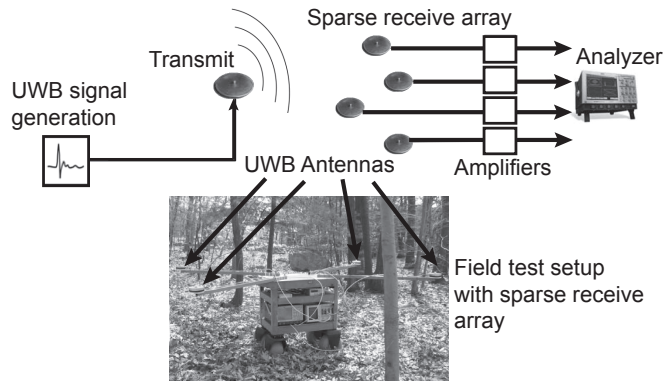


**Figure 4.12** Diagram and photograph showing an ultrawideband field test setup with conical monopole antennas for transmit and receive [23].

array configurations are of general interest such as linear or two-dimensional arrays of ultrawideband conical monopoles, which impacts the design of the individual array elements.

The terms wideband, very wideband, and ultrawideband (as commonly used in the literature) are understood here to be equivalent. A number of ultrawideband applications have received FCC approval for use as described in Federal Communications Commission document FCC 02-48, First Report and Order, Revision of Part 15 of the Commission's Rules Regarding Ultra-Wideband Transmission Systems, Adopted February 14, 2002, Release date April 22, 2002 [27]. The 3.1 to 10.6 GHz band allocated by the FCC for ultrawideband communications is a possible application for the antenna described in the first example given in this chapter. For example, an ultrawideband signal (pulse position modulation (PPM) or orthogonal frequency division multiplex (OFDM)) or multiple RF signals over an ultrawideband would be applied across the antenna feed gap region, inducing a time-varying current that gives rise to electromagnetic radiation for wireless transmission. For wireless ultrawideband reception, an incident time-varying electromagnetic wave signal induces a time-varying electric current on the monocone and a time-varying voltage across the antenna feed gap.

A design of a linearly polarized ultrawideband antenna element capable of operating over the instantaneous 3.1 to 10.6 GHz band for receive and/or transmit wireless communications applications is described in the next

subsection. The design uses a conical monopole on a circular ground plane with a number of practical features for indoor and outdoor use.

#### 4.2.3 Prototype 1: Monocone Antenna for the 3.1 GHz to 10.6 GHz Band

Referring to the diagram of a conical monopole antenna shown in Figure 4.6, the following parameters allow good performance over the 3.1 GHz to 10.6 GHz instantaneous band. It has been assumed that the coaxial feedline for the monocone is a standard SMA connector, where the center conductor has a diameter equal to 0.127 cm [0.050 inches]. The base diameter of the cone then is chosen as 0.254 cm [0.1 inches], which allows a threaded center conductor of the SMA connector to be attached within a corresponding tapped hole in the cone base region. For prototype testing, the conical monopole is made of solid brass with a flat top and a flat base region. The cross section of the monopole is circular for ease of machining and to achieve omnidirectional azimuthal coverage. A standard SMA connector (4-hole flange mount jack receptacle) with a modified center pin that was threaded made the RF antenna connection via a threaded hole in the conical monopole. Thus, solder was not required for this fabricated antenna. The SMA connector introduces a 1.27 cm [0.5 inches] length of teflon-loaded coaxial line. The moment method simulation includes the same 1.27 cm length of teflon-loaded coaxial line. For antenna testing, a 15.24 cm [6 inch] diameter circular aluminum plate 0.3175 cm [0.125 inch] thick was used as the ground plane - the simulation model used a perfectly conducting ground plane with the same diameter. A photograph of the fabricated conical monopole antenna (prototype 1) is shown in Figure 4.13.



**Figure 4.13** Photograph of a conical monopole over a circular ground plane, designed for the 3.1 to 10.6 GHz band (prototype 1).

The height of the prototype 1 cone is 1.5 cm [0.59 inches], and the top truncation diameter is 1.2 cm [0.472 inches]. The full cone angle for this



design is  $35^\circ$ . At the lowest frequency 3.1 GHz, the wavelength is 9.68 cm [3.8 inches] and at the highest frequency 10.6 GHz the wavelength is 2.189 cm [1.11 inches]. The top truncation diameter varies from  $0.124\lambda$  at 3.1 GHz to  $0.425\lambda$  at 10.6 GHz. The height of the conical monopole varies from  $0.155\lambda$  at 3.1 GHz to  $0.53\lambda$  at 10.6 GHz. It should be noted that the conical monopole size in this design does not fit the simple model that could be used for infinite or electrically large cones, that is, the characteristic impedance, reflection coefficient, and VSWR shown in Figures 4.9 to 4.11, respectively, would not apply. Also, the cone half-angle of the conical monopole here is not large, so the finite cone theory of Papas and King [10, 11] would not be expected to apply. Instead, an initial estimate of the reflection coefficient and VSWR performance can be determined from measured input impedance data for finite cones provided by Brown and Woodward [15]. In terms of electrical degrees, the height of the conical monopole varies from  $55.8^\circ$  at 3.1 GHz, to  $107.8^\circ$  at 6 GHz, to  $190.8^\circ$  at 10.6 GHz. From the measured Brown and Woodward data in Figures 4.7 and 4.8, the estimated input impedance for this cone design varies from about  $30 - j10$  ohms at 3.1 GHz, to  $160 + j10$  ohms, at 6 GHz, to  $76 - j25$  ohms at 10.6 GHz. Note: these estimated input impedance values are referenced to the input coaxial feed region of the monocone. The corresponding reflection coefficient and VSWR for this case are computed from Equations (1.15) and (1.27), respectively, as  $(-11.1 \text{ dB}, 1.77)$  at 3.1 GHz,  $(-5.6 \text{ dB}, 3.2)$  at 6 GHz, and  $(11.0 \text{ dB}, 1.78)$  at 10.6 GHz.

An accurate calculation of the conical monopole input impedance versus frequency can be made using the method of moments, as shown by comparisons below with measured data for this antenna. The moment method simulation model for the 3.1 GHz to 10.6 GHz antenna design is shown in Figure 4.14. The simulation model includes a 1.27 cm long teflon-loaded coaxial feedline to model the SMA connector.

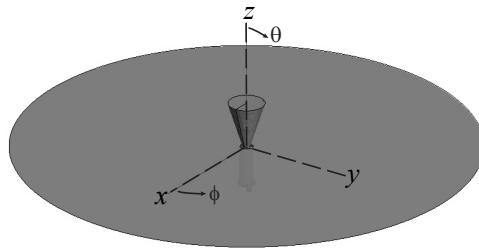


**Figure 4.14** Simulation model for a conical monopole over a 15.24 cm diameter circular ground plane fed with a coaxial line, designed for the 3.1 to 10.6 GHz band (prototype 1). Cone height 1.5 cm, cone full angle  $35^\circ$ .

The simulated directivity patterns of prototype 1 at 3.1 GHz, 6 GHz and 10.6 GHz are shown in Figure 4.15. Figure 4.16 shows the simulated directivity versus frequency at the observation angle  $\theta = 90^\circ$ , and over the frequency band 3.1 GHz to 10.6 GHz there is less than 2 dB variation in directivity. A comparison of the simulated and measured input resistance

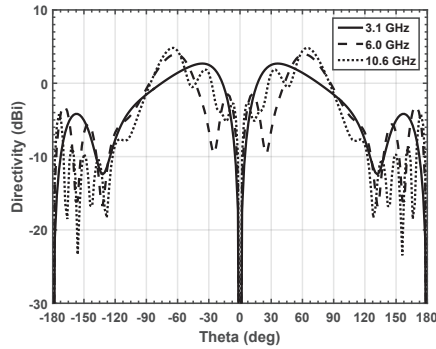


**Figure 4.15** Simulated directivity patterns for a conical monopole over a circular ground plane (prototype 1).

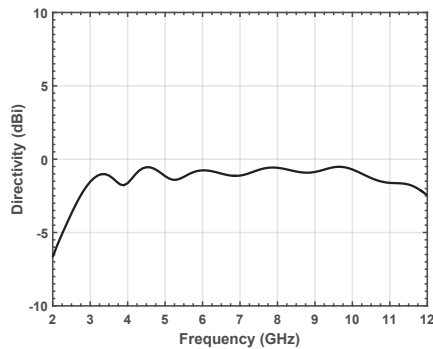


**Figure 4.16** Simulated directivity versus frequency at  $\theta = 90^\circ$  for a conical monopole over a circular ground plane (prototype 1).

and input reactance versus frequency are shown in Figures 4.17 and 4.18, respectively, and generally good agreement is observed. Note: that the reference plane here is at the input to the SMA connector. Although not shown here, if the input impedance data (in Figures 4.17 and 4.18) at the input to the SMA connector were transformed to a reference position at the ground plane, they would tend to look more like the measured impedance data shown in Figures 4.7 and 4.8. In the desired frequency range of 3.1 GHz

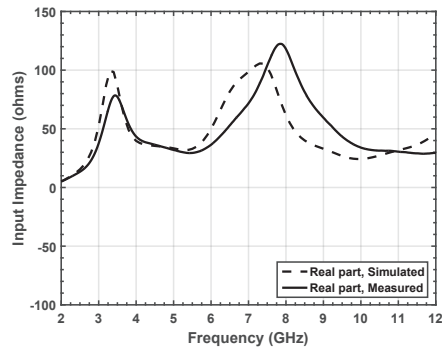


**Figure 4.17** Simulated and measured input impedance (real part) for the conical monopole over a circular ground plane, fed with a coaxial line (prototype 1). The reference plane is at the input to the SMA connector.

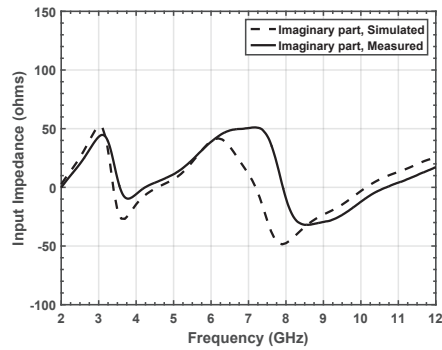


**Figure 4.18** Simulated and measured input impedance (imaginary part) for the prototype 1 conical monopole over a circular ground plane, fed with a coaxial line. The reference plane is at the input to the SMA connector.

to 10.6 GHz, the measured input resistance has two peaks occurring near 3.5 GHz (79 ohms) and 7.8 GHz (123 ohms). The corresponding simulated and measured reflection coefficient, VSWR, and mismatch loss are shown in Figure 4.19 to 4.21, respectively, and good agreement is observed. The measured and simulated reflection coefficient minimum occurs at 4 GHz and 4.25 GHz, respectively. The measured VSWR is less than about 2.5:1 over the 3.1 GHz to 10.6 GHz band. Figure 4.21 shows that the measured mismatch loss due to impedance mismatch is less than 1 dB over the desired band.

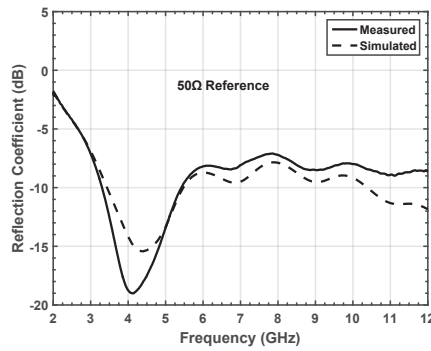


**Figure 4.19** Simulated and measured reflection coefficient for a conical monopole over a circular ground plane, fed with a coaxial line (prototype 1).

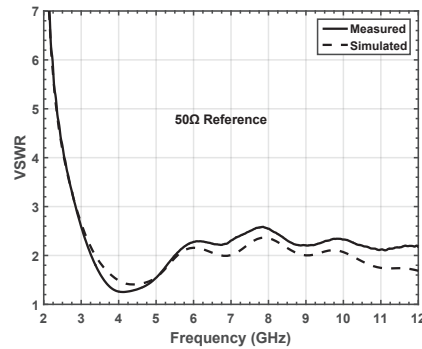


**Figure 4.20** Simulated and measured VSWR for a conical monopole over a circular ground plane, fed with a coaxial line (prototype 1).

#### 4.2.4 Prototype 2: Moncone Antenna for X-Band, 8 GHz to 12 GHz

As a second example, consider the design of a conical monopole to cover the X-band frequency range 8 GHz to 12 GHz. A photograph of the prototype 2 X-band conical monopole antenna is shown in Figure 4.22 and the corresponding simulation model is shown in Figure 4.23. The design parameters have been chosen to allow the element to be arranged either as a single element or in an array of conical monopoles over a ground plane. The height of the cone is 0.635 cm [0.25 inches], and the top truncation diameter is 0.508 cm [0.2 inches]. The base of the cone is 0.254 cm [0.1 inches]. The full cone angle for this design is  $22.6^\circ$ . At the lowest frequency 8 GHz, the wavelength is 3.75 cm [1.48 inches] and at the highest frequency 12 GHz the wavelength

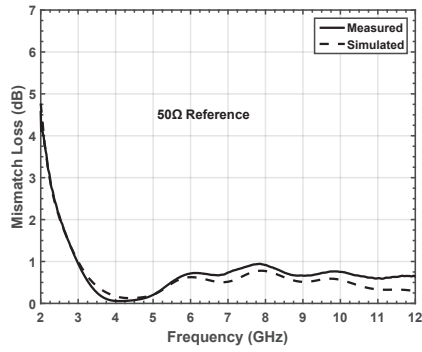


**Figure 4.21** Simulated and measured mismatch loss for a conical monopole over a circular ground plane, fed with a coaxial line (prototype 1).

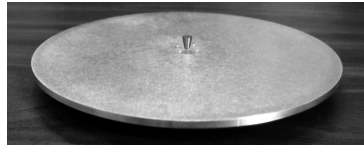


**Figure 4.22** Photograph of an X-band conical monopole over a circular ground plane (prototype 2).

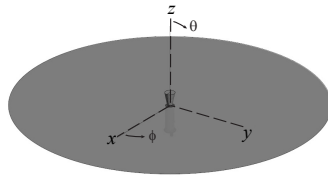


**Figure 4.23** Simulation model for an X-band conical monopole over a circular ground plane (prototype 2).

is 2.5 cm [0.984 inches]. The top truncation diameter varies from  $0.135\lambda$  at 8 GHz to  $0.2\lambda$  at 12 GHz. The height of the conical monopole varies from  $0.169\lambda$  at 8 GHz to  $0.25\lambda$  at 12 GHz. It should be noted that the conical monopole size in this design does not fit the simple model that could be used for electrically larger cones, that is, the characteristic impedance, reflection coefficient, and VSWR shown in Figures 4.9 to 4.11, respectively, would not apply. Instead, an initial estimate of performance can be determined from measured input impedance data for finite cones provided by Brown and Woodward [15]. In terms of electrical degrees, the height of the conical monopole varies from  $60.8^\circ$  at 8 GHz, to  $76.2^\circ$  at 10 GHz, to  $90^\circ$  at 12 GHz.

From the measured Brown and Woodward data in Figures 4.7 and 4.8, the estimated input impedance for this cone design varies from about  $30 + j10$  ohms at 8 GHz, to  $70 + j40$  ohms, at 10 GHz, to  $120 + j60$  ohms at 12 GHz. The corresponding estimated reflection coefficient and VSWR for this case (assuming a 50-ohm feedline) are computed from Equations (1.15) and (1.27), respectively, as (-11.1 dB, 1.77) at 8 GHz, (-9 dB, 2.1) at 10 GHz, and (-5.8 dB, 3.1) at 12 GHz.

A comparison of the prototype 2 measured and simulated input impedance is shown in Figures 4.24 (input resistance) and 4.25 (input reactance), and good agreement is observed. Over the 8 to 12 GHz band,

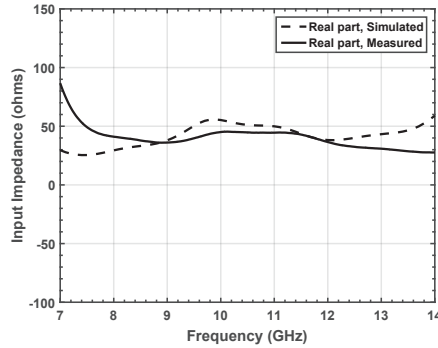


**Figure 4.24** Simulated and measured input resistance of an X-band conical monopole over a circular ground plane (prototype 2). The reference plane is at the input to the SMA connector.

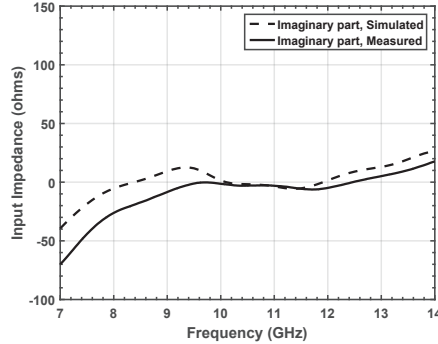


**Figure 4.25** Simulated and measured input reactance of an X-band conical monopole over a circular ground plane (prototype 2). The reference plane is at the input to the SMA connector.

the input resistance is in the range of about 35 ohms to 45 ohms and the

input reactance is in the range of about  $-25$  ohms to  $0$  ohms. The measured and simulated reflection coefficient were computed from the input impedance using a  $50$ -ohm reference and good agreement is observed. The reflection coefficient magnitude is less than  $-10$  dB over the  $8$  to  $12$  GHz band. In

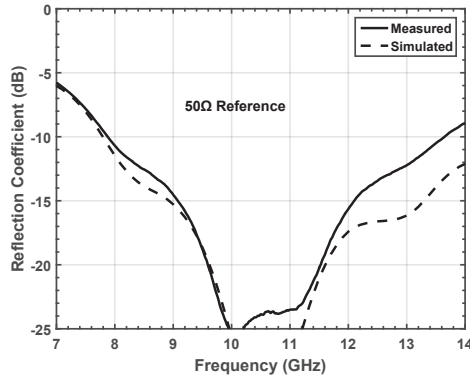


**Figure 4.26** Simulated and measured reflection coefficient for an X-band conical monopole fed with a coaxial line (prototype 2).

Figure 4.27, the measured VSWR is observed to be less than  $1.75$  over the  $8$  to  $12$  GHz band, and in Figure 4.28 the mismatch loss is less than  $0.4$  dB.

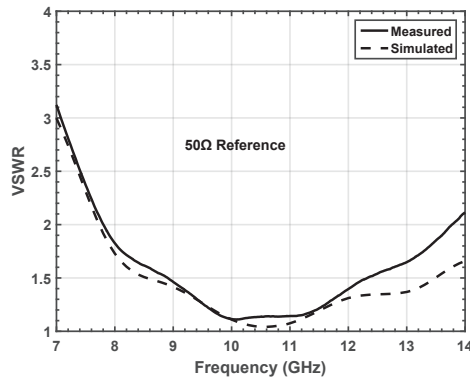


**Figure 4.27** Simulated and measured VSWR for an X-band conical monopole over a circular ground plane, fed with a coaxial line (prototype 2).

#### 4.2.5 Prototype 3: Monocone Array for X-Band, 8 GHz to 12 GHz

The prototype 2 conical monopole was mounted in a four-element linear array (referred to as prototype 3) with  $1.27$  cm [ $0.5$  inches] element spacing,

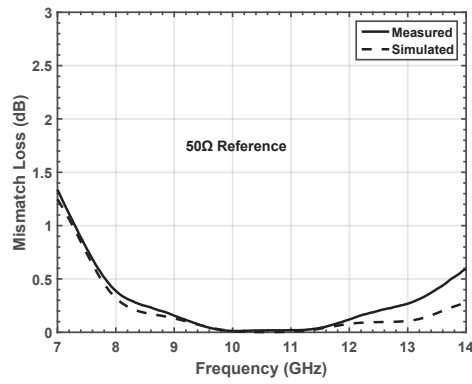


**Figure 4.28** Simulated and measured mismatch loss for an X-band conical monopole over a circular ground plane, fed with a coaxial line (prototype 2).

centered on a 15.24 cm (6 inch) square aluminum ground plane. At 12 GHz, the array electrical spacing is  $0.508\lambda$ . A close-up view of the prototype 3 array is shown in Figure 4.29. The measured input impedance for a central

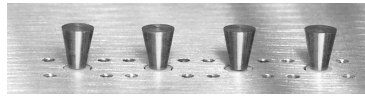


**Figure 4.29** Photograph of a 4-element X-band conical monopole linear array (prototype 3).

element of the prototype 3 array is shown in Figure 4.30. At 8 GHz, the

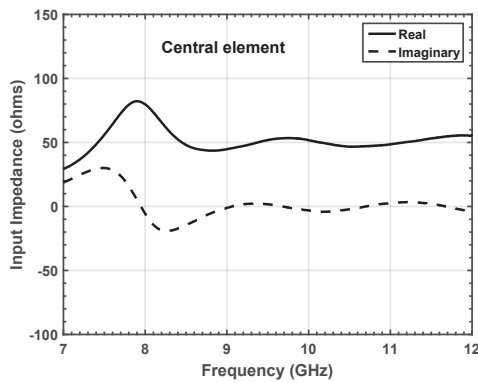


**Figure 4.30** Measured input impedance of a central element of the 4-element X-band conical monopole linear array over a ground plane (prototype 3).



input resistance is approximately 75 ohms and then quickly settles to around 50 ohms at 8.5 GHz and remains close to that value up to 12 GHz. The input reactance is close to 0 ohms over the entire band except near 8.25 GHz where the value is approximately  $-20$  ohms. As shown in Figure 4.31, the measured VSWR is less than 1.6 over the 8 to 12 GHz band.

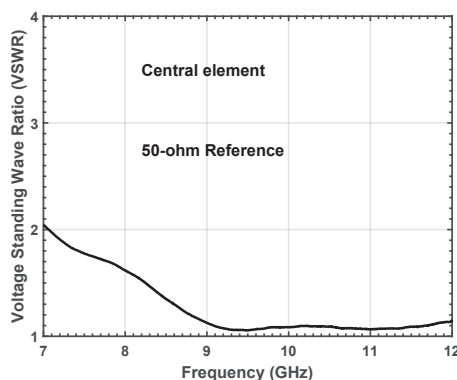


**Figure 4.31** Measured VSWR of a central element of the 4-element X-band conical monopole linear array over a ground plane (prototype 3).

### 4.3 Wire Discone Antenna with Cylindrical Monopole

The previous sections discussed cone antennas and ground planes made of a solid material. For lower frequencies such as VHF, where the cone antennas and ground plane become physically large and heavy, it is desirable to approximate the cone and ground plane geometries with metallic wires that form an outline of the cone and ground plane. An omnidirectional vertically-polarized discone [28–36] antenna design involves a cone fed against a circular disc, where the disc diameter is similar in size to the diameter of the cone. Discone antennas are designed in a number of ways: such as a cone with disc, cone with disc and tuning coil, cone and disc with tuning coil and thin monopole (whip) antenna. The tuning coil helps to achieve a lower frequency response and can consist of a helical conductor connecting the disc section and the monopole. In the example shown here, the discone antenna uses a large diameter monopole instead of a thin whip, and a tuning coil is not used. An example of a modified wire discone antenna for VHF operation is depicted in a simulation model shown in Figure 4.32. A photograph of the fabricated wire discone antenna integrated with the cylindrical monopole that was mounted on a vertical mast is shown in Figure 4.33. A close-up view of the antenna feed

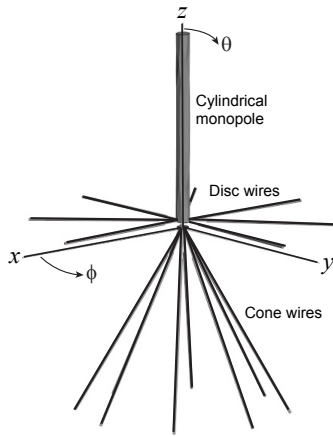


**Figure 4.32** Simulation model of a wire discone antenna with a vertical monopole.

region is depicted in Figure 4.34, which shows the lower part of the cylindrical monopole, the disc wires, upper hub, insulator, lower hub, and cone wires.



**Figure 4.33** Photograph of a wire discone antenna with a cylindrical monopole.

The antenna was designed to have a VSWR less than 2.5 over the frequency band 150 MHz to 230 MHz. In this design, there are eight (8) radial wires that approximate a disc and eight (8) radial wires that approximate a cone. The radial disc wires are 27.305 cm long and 0.368 cm diameter, and the radial cone wires are 38.1 cm long and 0.48 cm diameter. The cylindrical monopole is 34.29 cm long and 2.86 cm diameter. These lengths were determined by

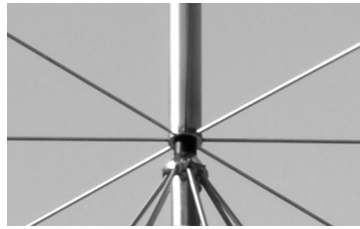


**Figure 4.34** Photograph showing a close-up view of the feed region for a wire disccone antenna integrated with a cylindrical monopole.

simulations with the FEKO moment method solver. At the high frequency, 230 MHz, the wavelength is 1.3m so the radial disc wires are  $0.21\lambda$ , the radial cone wires are  $0.29\lambda$ , and the monopole is  $0.26\lambda$ . The simulated and measured voltage standing wave ratio (VSWR) of the wire disccone with cylindrical monopole antenna is shown in Figure 4.35 and good agreement is observed.

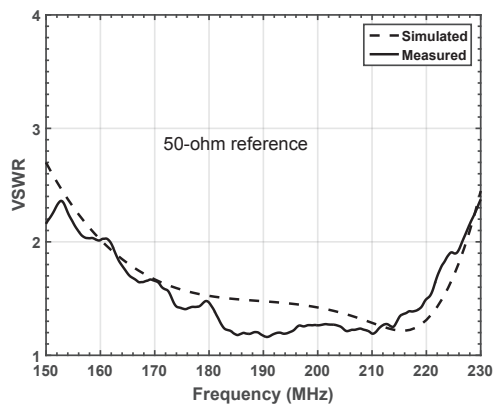


**Figure 4.35** Comparison of the simulated and measured VSWR for a wire disccone antenna with a cylindrical monopole.

#### 4.4 Monopole Array for Simultaneous Transmit and Receive

This section describes an antenna array composed of an omnidirectional 8-element transmit array and a central receive antenna, for operation in the 2.4 to 2.5 GHz Industrial, Scientific, and Medical (ISM) radio band. A diagram of this array is shown in Figure 4.36. This array has been developed for simultaneous transmit and receive (STAR) applications for wireless

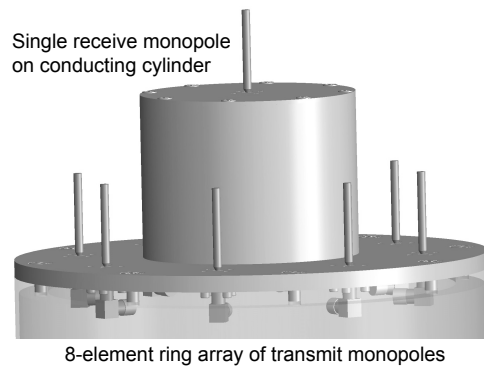


**Figure 4.36** Diagram of a monopole transmit array and monopole receive antenna for simultaneous transmit and receive application.

communications that require high isolation between transmit and receive functions [36, 37]. The transmit antenna array has eight monopole radiating antenna elements uniformly spaced on a ring. The transmit monopole antenna elements are approximately one-quarter wavelength long at the center frequency and they are oriented perpendicular to an electrically conducting circular ground plane. The transmit monopole array elements are uniformly spaced approximately one-half wavelength apart, and they are each driven at a position approximately one-quarter wavelength in front of a central electrically conducting circular cylinder. Referring to the phasing diagram in Figure 4.37, the transmit monopoles are phased with a linear progressive phase shift between elements to cover 0 to 360 degrees around the ring array, such that opposing transmit elements are 180 degrees out of phase creating a near-field null on the axis of the ring array. With this type of

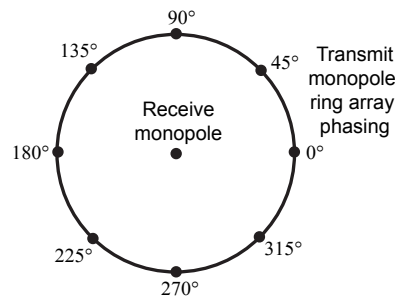


**Figure 4.37** Phasing diagram for a transmit monopole ring array and monopole receive antenna for simultaneous transmit and receive application.

linear progressive phase distribution, the transmit array far-field radiation

pattern has an omnidirectional (constant) magnitude in azimuth. It is known from the literature that a ring array antenna with a linear phase progression covering a full 360 degrees around the array circumference will produce an omnidirectional radiation pattern, as described by Rudge [38]. In the case where there is an even number of elements in the ring array and each opposing pair is fed anti-phase or with a 180 degree phase shift, there will be a radiation pattern null formed at the midpoint of the array. This ring array midpoint nulling effect is recognized for monopole arrays and other types of antennas with application to simultaneous transmit and receive. A ring array of four progressively phased (0, 90, 180, 270 degrees) dipole antenna elements and a central dipole for improved isolation has been investigated by simulations and measurements by Chiang [39].

In the antenna design described here, to achieve high isolation between transmit and receive antennas, the receive antenna is centrally located on the axis of the transmit ring array and it is elevated, into the shadow zone [40] of the transmit array antennas, on a circular ground plane above the transmit array. In this design, there is no direct ray path from the transmit array monopole elements and the receive monopole element, so the only mutual coupling is due to edge diffraction. The transmit array is designed to operate over a circular ground plane or within a parallel plate radial waveguide. A prototype STAR monopole antenna array has been fabricated as shown in Figure 4.38. In this design, the transmit and receive monopoles each have a

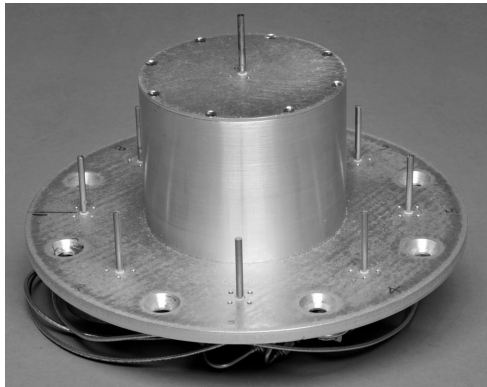


**Figure 4.38** Photograph of a monopole transmit array and monopole receive antenna for simultaneous transmit and receive application.

length 3.048 cm [1.2 inches] and diameter 0.3175 cm [0.125 inches]. The transmit array has eight monopole arranged in a ring array with diameter 15.68 cm [6.172 inches] that is mounted on an aluminum ground plane with diameter 21.234 cm [8.36 inches]. The receive monopole is mounted on the

top of a closed-end aluminum cylinder with height 7.315 cm [2.88 inches] and outside diameter 9.672 cm [3.808 inches]. The transmit array beamforming was accomplished with analog components as follows. The input signal to the transmit array was divided by a 4-way power divider, and compared to a reference coaxial cable length of 0 degrees, coaxial adapters approximating relative phases of 45, 90, and 135 degrees were used. The four phase-delayed signal paths were then further divided using 180-degree hybrids to generate the desired progressive phase variation of 0, 45, 90, 135, 180, 225, 270, 315 degrees for the eight-element transmit ring array. The array was tested in an anechoic chamber and provides high isolation on the order of 55 to 60 dB, as described below. The measured results are summarized in Figures 4.39 to 4.42. The measured reflection coefficient at the input port of the 8-way

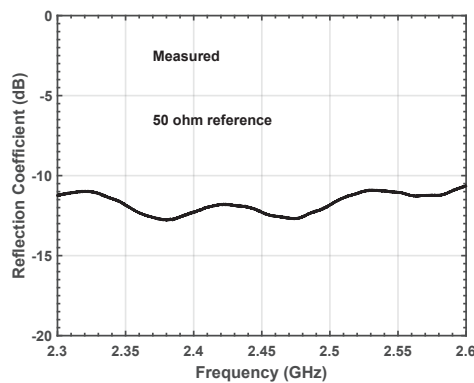


**Figure 4.39** Measured reflection coefficient for a monopole transmit array for simultaneous transmit and receive application.

beamformer of the transmit phased array is shown in Figure 4.39. Over the 2.4 GHz to 2.5 GHz ISM band the measured reflection coefficient magnitude is less than  $-12$  dB. As shown in Figure 4.40, the measured mutual coupling between the monopole transmit array and the central monopole receive antenna is less than  $-56$  dB over the 2.4 GHz to 2.5 GHz band. The measured far-field vertically polarized azimuth gain patterns of the transmit phased array are shown in Figure 4.41, which demonstrates an approximate omnidirectional characteristic. In Figure 4.42 as expected, due to the progressive phase steering, the measured far-field azimuth phase patterns for the monopole transmit array demonstrate the 0 to  $360^\circ$  azimuthal phase shift.

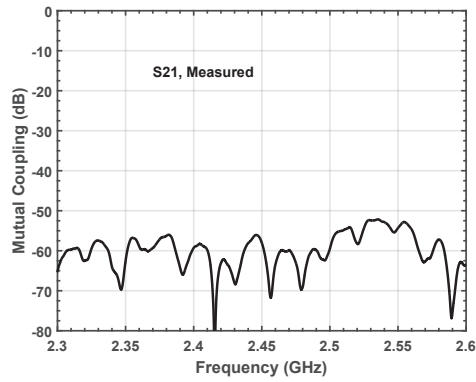


**Figure 4.40** Measured mutual coupling ( $S_{21}$ ) between a monopole transmit array and monopole receive antenna for simultaneous transmit and receive application.

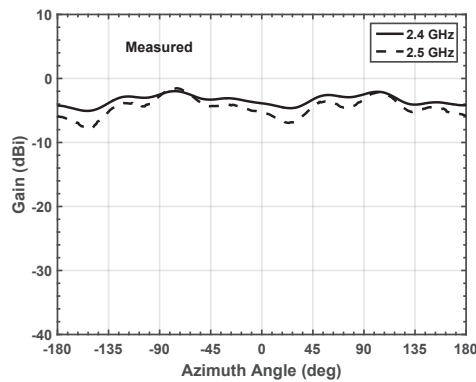


**Figure 4.41** Measured far-field azimuth gain patterns for a monopole transmit array for simultaneous transmit and receive application.

## 4.5 Horizontal Loop and Slotted Cylinder Antennas

Omnidirectional horizontal polarization can be generated in a number of ways. For example a photograph of a horizontal uniform current loop such as an Alford loop antenna [41–47] is shown in Figure 4.43. In this photograph a standard semi-rigid coaxial cable is used to feed a two-way radial power divider implemented on a PC board with etched transmission lines on each side of the board. The spacing between the transmission lines is chosen to achieve a desired characteristic impedance. Each arm of the radial power divider feeds a V-dipole, and the two V-dipoles for an approximate uniform

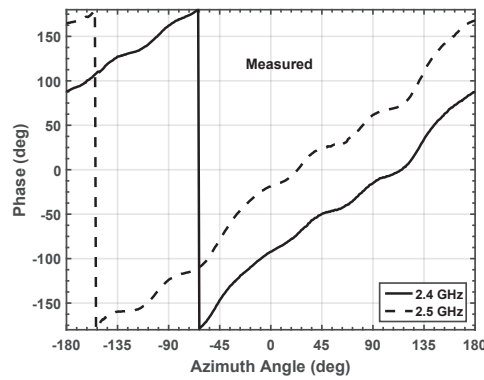


**Figure 4.42** Measured far-field azimuth phase patterns for a monopole transmit array for simultaneous transmit and receive application.

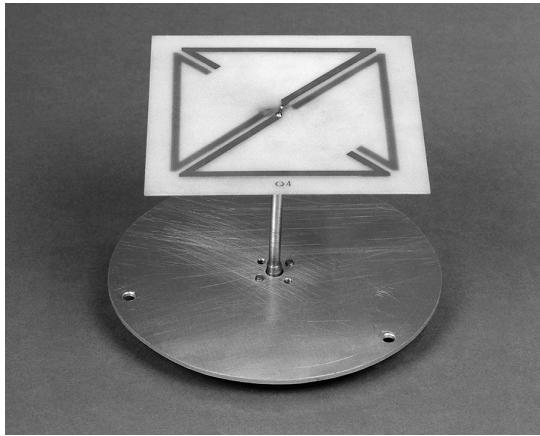


**Figure 4.43** Photograph of an Alford-type uniform current loop antenna.

current loop. The example shown has a square perimeter, but a circular loop is also possible. With two feeds, the typical loop perimeter length for resonance is on the order of one wavelength. Mutual coupling effects are substantial with these close proximity V-dipoles. To achieve a desired impedance match, in capacitively coupled tuning stubs are included at the tips of the V-dipoles. An improved impedance match can be achieved by tapering the ends of the V-dipoles to a sharp tip. As the perimeter of the loop increases, additional feed points are required to maintain an approximate uniform loop current. For example, when the loop perimeter is on the order of two wavelengths four feedpoints are needed.

An alternate configuration surrounds the uniform current loop with a



metallic cylinder with vertical slots as depicted in the artist's concept shown in Figure 4.44. The resonance of the antenna is controlled by the slot width and

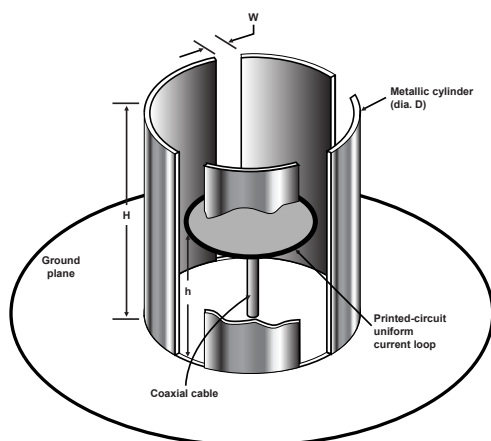


**Figure 4.44** Artist's concept of a loop-fed slotted cylinder antenna.

by the diameter and height of the cylinder. Typical dimensions for resonance (determined empirically) are cylinder height  $H = 0.425\lambda$ , cylinder diameter  $D = 0.35\lambda$ , and slot width  $W = 0.04\lambda$ . With either the uniform current loop or the loop-fed slot cylinder, the radiation pattern of an embedded element remains omnidirectional in the presence of other like elements in a planar phased array configuration.

In applications, where additional gain is required in the vertical dimensions it is possible to stack slotted cylinder antennas in a co-linear array fashion. Figure 4.45 depicts a diagram of an example UHF two-element co-linear array of slotted cylinder antennas with three slots per element. To feed the two sets of three slots, two coaxial cables could be run along the central axis of the slotted cylinders, and then each of the coaxial cables would be connected to three-way power dividers that provide the necessary transmission lines to feed the three slots. Each slot could then be fed by connecting the outer conductor of the coaxial line to one side of the slot and the center pin to the other side of the slot. An alternate approach to feeding the slots is to use a transformer balun. A photograph of the UHF two-element colinear array of horizontally polarized slotted cylinder antennas is shown in Figure 4.46. The measured impedance mismatch loss is shown in Figure 4.47. The measured horizontally polarized omnidirectional gain patterns are shown in Figure 4.48.

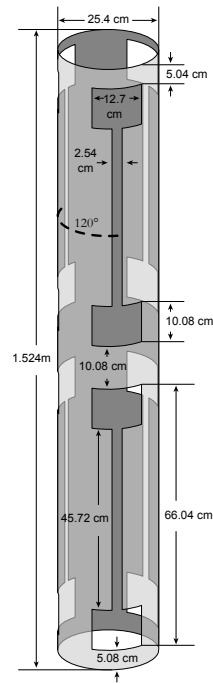


**Figure 4.45** Drawing of a UHF two-element colinear array of horizontally polarized slotted cylinder antennas.

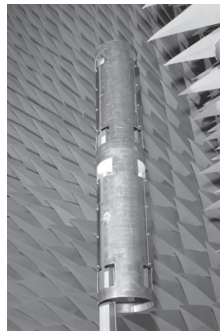


**Figure 4.46** Photograph of a UHF two-element colinear array of horizontally polarized slotted cylinder antennas.

## 4.6 Turnstile Antenna With Crossed V-Dipoles

The turnstile antenna [48] was discussed briefly in Chapter 1 (Section 1.12.2) where crossed Hertzian (short) dipoles with a  $90^\circ$  phase shift between the

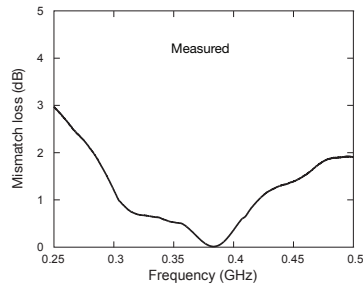


**Figure 4.47** Measured impedance mismatch loss of the UHF two-element colinear array of horizontally polarized slotted cylinder antennas.

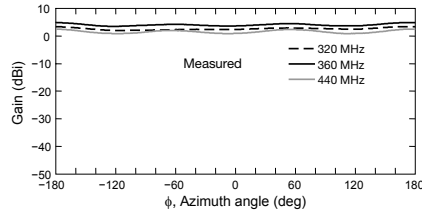


**Figure 4.48** Measured horizontally polarized omnidirectional gain pattern of the UHF two-element colinear array of slotted cylinder antennas.

arms was used to generate an omnidirectional radiation pattern. In this section, a practical turnstile dipole antenna is described. A wideband UHF dual-polarized dipole antenna with swept-back arms and folded balun over a ground plane in free space was described in Chapter 3 (refer to Figure 3.6), and the same design is analyzed here as a turnstile antenna. The simulation model is shown in Figure 4.49. The dipole arm length was chosen as 13.4 cm, which is  $0.268\lambda$  at 600 MHz (center frequency). The dipole arms and balun sections are modeled as 1.42 cm diameter ( $D$  in Figure 3.1) perfectly conducting tubes. The dipole height is chosen as 17.9 cm ( $H$  in Figure 3.1) so that at the center frequency, the height at the midpoint of the dipole arm is approximately  $\lambda/4$  over the ground plane. A circular ground plane with diameter 45.72 cm is used here. The folded balun tubes are spaced 3.81 cm center to center ( $s$  in Figure 3.1), which by Equation (3.1) provides a  $197\Omega$  characteristic impedance transmission line. The folded balun provides mechanical support of the dipole arms and is short circuited at the ground plane. Electrically, this balun behaves as a purely reactive impedance in parallel with the dipole feed terminals. One of the balun tubes contains a coaxial line that is connected to the dipole terminals using a crossover connection located 1.27 cm ( $h$  in Figure 3.1) above the top of the folded

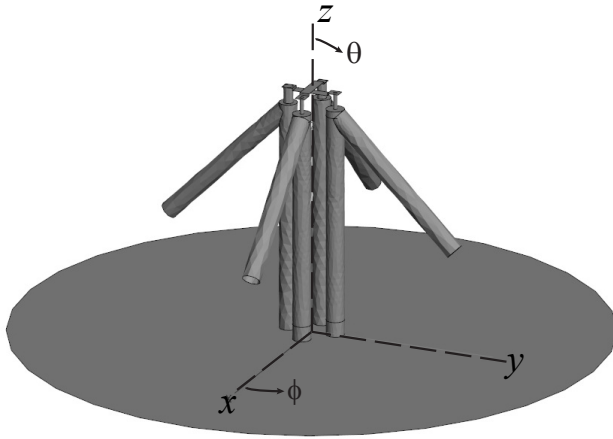


**Figure 4.49** Simulation model for a UHF turnstile antenna composed of crossed V-dipoles over a ground plane.

balun. Figure 4.50 shows the azimuth gain patterns in the  $xy$  plane at 450 MHz for vertical and horizontal polarizations. The horizontal component is at

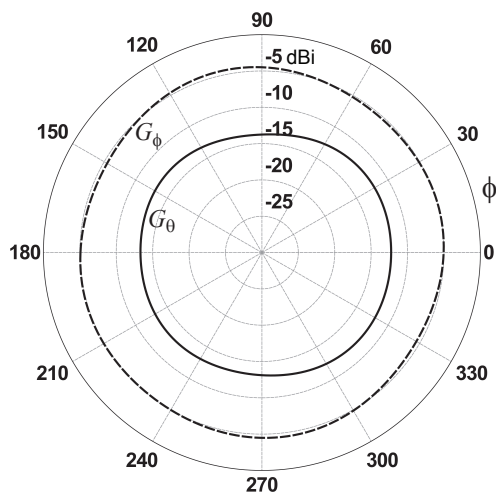


**Figure 4.50** Simulated azimuth gain patterns at 450 MHz for a UHF turnstile antenna composed of crossed V-dipoles over a ground plane.

the  $-5$  dBi level. If the arms were not swept back, this horizontal component would be closer to the  $-2$  dBi level. The vertical component is on the order

of  $-12.5$  dBi, and would otherwise be negligible if the arms were not swept back.

## 4.7 Summary

This chapter has described simulations and measurements of antennas that are omnidirectional in azimuth. Omnidirectional coverage can be provided for vertical polarization with vertical monopole or dipole antennas which can typically have a cylindrical or conical shape. Similarly, a dipole antenna with cone-shaped arms is referred to as a bicone or biconical antenna. A monopole ring array with progressive phasing can generate omnidirectional far-field radiation patterns for simultaneous transmit and receive. Omnidirectional horizontally polarized coverage can be achieved with horizontal loops or slotted cylinder antennas. The next chapter also discusses loop antennas, but in a configuration of multiple orthogonal loops as a vector sensor antenna for direction finding application.

## References

- [1] J.D. Kraus, *Antennas*. New York: McGraw-Hill, 1950.
- [2] S.A. Schelkunoff and H.T. Friis, *Antennas: Theory and Practice*. New York: Wiley, 1952.
- [3] W.L. Stutzman and G.A. Thiele, *Antenna Theory and Design, 2nd ed.* New York: Wiley, 1998.
- [4] J. Volakis, ed., *Antenna Engineering Handbook, 4th ed.* New York: McGraw-Hill, 2007.
- [5] C.A. Balanis, *Antenna Theory, Analysis and Design, 3rd ed.* New York: Wiley, 2005.
- [6] H.J. Reich, ed., *Very High Frequency Techniques, vol. 1*, New York: McGraw-Hill, 1947.
- [7] S.A. Schelkunoff, *Advanced Antenna Theory*, New York: Wiley, 1952.
- [8] S.A. Schelkunoff, "General Theory of Symmetric Biconical Antennas," *J. of Applied Physics*, vol. 22, no. 11, Nov. 1951, pp. 330–332.
- [9] C.T. Tai, "On the Theory of Biconical Antennas," *J. Appl. Phys.*, vol. 19, , Dec. 1948, pp. 1155–1160.
- [10] C. H. Papas and R. King, "Input Impedance of Wide-Angle Conical Antennas Fed By a Coaxial Line," *Proc. I.R.E.* , vol. 39, Nov. 1949, pp. 1269–1271.
- [11] C.H. Papas and R. King, "Input Impedance of Wide-Angle Conical Antennas," Harvard University, Cruft Laboratory, Technical Report No. 52, Dec. 1, 1948.
- [12] C.H. Papas and R.W.P. King, "Radiation from Wide-Angle Conical Antennas Fed by a Coaxial Line," *Proc. I.R.E.*, vol. 39, Jan 1951, pp. 49–51.

- [13] P.D.P. Smith, "The Conical Dipole of Wide Angle," *J. Appl. Physics*, vol. 19, January, 1948, pp. 11–23.
- [14] P.D.P. Smith, "Ground Plane Field of the Wide Angle Conical Dipole," *J. Appl. Phys.*, vol. 20, p. 636
- [15] G.H. Brown and O.M. Woodward, Jr., "Experimentally Determined Radiation Characteristics of Conical and Triangular Antennas," *RCA Review*, Vol. 13, December, 1952, pp. 425–452.
- [16] S. A. Schelkunoff, "Theory of Antennas of Arbitrary Size and Shape," *Proc. I.R.E.*, vol. 29, April 1941, pp. 493–521.
- [17] C.T. Tai, "Application of a Variational Principle to Biconical Antennas," *J. Appl. Phys.*, vol. 20, 1948, pp. 1076–1084.
- [18] D. N. Black and T. A. Brunasso, "An Ultra Wideband Bicone Antenna," *IEEE International Conference on Ultra-Wideband*, 2006, 15 January, 2007.
- [19] J.E. Lawrance, "The Fundamental Resonant Frequency and Radiation Characteristics of Wide Angle Conical Antennas," Thesis, Univ. of New Mexico, 2010.
- [20] M. Gardill, G. Fischer, R. Weigel, A. Koelpin, "Design of a Robust and Low-Cost Monocone Antenna Element for Use in Vehicle Roof-Mounted Antenna Arrays," *Radio and Wireless Symposium*, 2013, pp. 112–114.
- [21] A.J. Fenn, "Theoretical and Experimental Study of Monopole Phased Array Antennas," *IEEE Trans. Antennas and Propagation*, vol. 34, no. 10, 1985, pp. 1118–1126.
- [22] G.H. Brown and O.M. Woodward, Jr., "Experimentally Determined Impedance Characteristics of Cylindrical Antennas," *IRE Proc.*, vol. 33, 1945, pp. 257–262.
- [23] C.M. Keller, and D.P. Young, "Ultra-Wideband (UWB) Signal Localization Using a Vehicle-Sized Array," *2005 IEEE International Conference on Ultra-Wideband*, 2005, pp. 290–295.
- [24] R.H.T. Bates and G.A. Burrell, "Towards Faithful Radio Transmission of Very Wide Bandwidth Signals," *IEEE Transactions on Antennas and Propagation*, Vol. 20, No. 6, November 1972, pp. 684 – 690.
- [25] J.G. Maloney, B.L. Shirley, and G.S. Smith, "Physical Description for the Reception of Short Pulses by Antennas," *1994 Antennas and Propagation Society International Symposium, AP-S. Digest*, Vol. 3, 1994, pp. 1790-1793.
- [26] J.D. Kraus, *Antennas*, 2nd Edition, New York: McGraw-Hill, 1988, p. 355.
- [27] FCC 02-48, First Report and Order, Revision of Part 15 of the Commission's Rules Regarding Ultra-Wideband Transmission Systems, Federal Communications Commission, Adopted February 14, 2002, Release date April 22, 2002.
- [28] A.G. Kandoian, "Three New Antenna Types and Their Applications," *Proc. IRE*, vol. 34, Feb. 1946, pp. 70W-75W.
- [29] R.A. Burberry, *VHF and UHF Antennas*, London: Peter Perigrinus, Ltd., 1992.
- [30] M. Dionigi, M. Mongiardo, C. Tomassoni, Investigation on the Phase Center of Ultra

- Wideband Discone Antennas, *German Microwave Conference Digest of Papers*, 2010 pp. 59–62.
- [31] W. Yan, A. Chen, T. Jiang, “Design of UHF Miniature Discone Antenna,” *Proc. 9th Int. Symp. on Antennas, Propagation and EM Theory*, 2010, pp. 356–358.
  - [32] A. Chen, T. Jiang, Z. Chen, D. Su; Wenxuan Wei; Yanjun Zhang “A Wideband VHF/UHF Discone-Based Antenna,” *IEEE Antennas and Wireless Propagation Letters*, vol. 10, 2011, pp. 450–453,
  - [33] S. Verma, A. Mishra, R. Khan, “Analysis of Variation of Various Parameters on Design of Discone Antenna,” *IEEE Applied Electromagnetics Conference (AEMC)*, 2011, pp. 1–6.
  - [34] R. Goncalves, P. Pinho, N.B. Carvalho, “Design and Implementation of a 3D Printed Discone Antenna for TV Broadcasting System,” *IEEE Int. Symp. on Antennas and Propagation & USNC/URSI National Radio Science Meeting*, 2015, pp. 314–315.
  - [35] Y. Zhao, W. Wang, “Design of a Novel Broadband Skeletal Discone Antenna With a Compact Configuration,” *IEEE Antennas and Wireless Propagation Letters*, vol. 13, 2014, pp. 1725–1728.
  - [36] A.J. Fenn, P.T. Hurst, J.S. Herd, K.E. Kolodziej, L.I. Parad, H. Steyskal, “Simultaneous Transmit and Receive Antenna System”, United States Patent No. 8,749,441, June 10, 2014.
  - [37] K.E. Kolodziej, P.T. Hurst, A.J. Fenn, L.I. Parad, “Ring Array Antenna with Optimized Beamformer for Simultaneous Transmit and Receive,” *IEEE Int. Symp. on Antennas and Propagation*, Chicago, Illinois, July 2012, pp. 1–2.
  - [38] A.W. Rudge, *Handbook of Antenna Design*, London: Peter Peregrinus Ltd, 1983, vol. 2, pp. 305–329.
  - [39] B.A. Chiang, “A Study of Communication Antenna Isolation,” Final Report FAA-RD-73-94, Howard University, Washington, DC, June 1973, AD768848.
  - [40] R.G. Kouyoumjian and P.H. Pathak, “A Uniform Theory of Diffraction for an Edge in a Perfectly Conducting Surface,” *Proc. IEEE*, vol. 62, no. 11, Nov. 1974, pp. 1448–1461.
  - [41] Alford, A. and A. G. Kandoian, “Ultrahigh-Frequency Loop Antennas,” *Trans. AIEE*, vol. 59, 1940, pp. 843–848.
  - [42] S.R. Anderson, “VHF Omirange Accuracy Improvements,” *IEEE Trans. Aerospace and Navigational Elec.*, vol. 12, no. 1, 1965, pp. 26–35.
  - [43] D.L. Sengupta, “Theory of V.O.R. Antenna Radiation Patterns,” *Electron. Lett.*, Vol. 7, No. 15, 1971, pp. 418–420.
  - [44] Gupta, R.K., “On Radiation Properties of the Alford Loop and a Dipole Antenna,” *Proc. Inst. Elec. Eng. India*, 1971, pp. 145–150.
  - [45] A.J. Fenn, “Arrays of Horizontally Polarized Loop-Fed Slotted Cylinder Antennas,” *IEEE Trans. Antennas Propagat.*, Vol. 33, No. 4, 1985, pp. 375–382.
  - [46] T.A. Milligan, *Modern Antenna Design, 2nd ed.* Hoboken, NJ: Wiley-IEEE Press, 2005

- 
- [47] A.J. Fenn, *Adaptive Antennas and Phased Arrays for Radar and Communications*. Norwood, Mass.: Artech House, 2008.
- [48] G. Brown, "The Turnstile Antenna," *Electronics*, 1936.





# 5

## Vector Sensor Array Antennas

### 5.1 Introduction

Vector sensor array antenna systems can be used to measure multiple polarization components of an incident electromagnetic field [1–7]. Polarization diversity and spatial diversity offered by sparsely spaced multipolarized array elements can be useful in providing frequency reuse capability and in mitigating signal dropouts due to multipath or polarization mismatch for providing reliable data communications. Vector sensor array antenna systems provide the capability for receiving and processing linearly polarized, circularly polarized, elliptically polarized, partially polarized, and unpolarized fields. A vector sensor antenna that uses multipolarized diverse elements with diverse antenna gain patterns can be calibrated for determining angle of arrival for radiofrequency sources. A tripolarized antenna with three mutually perpendicular dipoles has been investigated for adaptive nulling applications [8]. This chapter describes the electromagnetic design of a vector sensor HF antenna array that could be integrated on a small satellite referred to in the literature as a nanosatellite or CubeSat [9]. A potential future application is for performing radio astronomy missions [9–16]. The antenna technology described here could be applied to other platforms such as airborne vehicles, towers, ground vehicles, and balloon-based applications [9, 17].

This chapter is organized as follows. In Section 5.2 some examples of vector sensor array prototype antennas are given. In Section 5.3, the operating modes of vector sensor antennas are described. In Section 5.4, vector sensor antenna design and simulated radiation patterns are given for potential application to galactic RF source mapping at HF from a nanosatellite. Section 5.5 presents a derivation of the received voltage matrix for a full six-mode vector sensor array antenna. Section 5.6 has a summary.

## 5.2 Background

There are various implementations of a full six-mode vector sensor antenna that include three orthogonal loop modes and three orthogonal dipole modes. In some applications with structural limitations, only a partial vector sensor antenna with less than six modes is practical – in this case multiple partial vector sensor antennas can be used to implement all six modes. Examples of full and partial vector sensor antenna prototypes are described below.

### 5.2.1 Prototype 1: Vector Sensor with Three Orthogonal Rings

An example of a full vector sensor antenna for radio astronomy [11] is depicted in the photograph shown in Figure 5.1. This electromagnetic vector

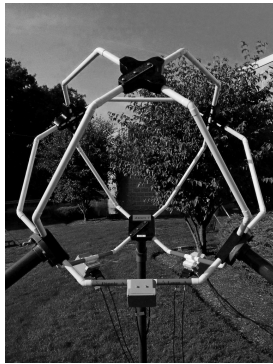


**Figure 5.1** Photograph of a full vector sensor antenna composed of three orthogonal dual-mode loops. Each loop has two ports that allow dipole and loop currents to be generated.

sensor was designed for ground-based measurements of galactic sources [11–15] within the HF and low VHF bands, and it is composed of three orthogonal rings approximately 1 m in diameter. At 30 MHz, the wavelength is 10 meters so the rings are considered electrically small ( $0.1\lambda$  diameter) and will have frequency independent radiation pattern shape. The rings are supported above the ground by three adjustable fiberglass legs. Each of the rings has two ports that are connected via a transformer balun and coaxial transmission lines within the ring's copper tubing to a sum and difference hybrid. The result is that each physical loop serves as both a dipole and a loop as will be described in Section 5.3. The full vector sensor array antenna produces six output channels allowing full characterization of the incident electromagnetic field. A ground-based HF vector sensor system consisting of three loops and three dipoles has also been developed by Lee et al [18].

### 5.2.2 Prototype 2: Array of Partial Vector Sensor Antennas

In some cases, only partial vector sensors may be practical. An example of a sparse array of partial vector sensor antennas installed on an unmanned air vehicle (UAV) [7] with electrically conducting wings is depicted in the photograph shown in Figure 5.2. In this photograph, there are crossed loops

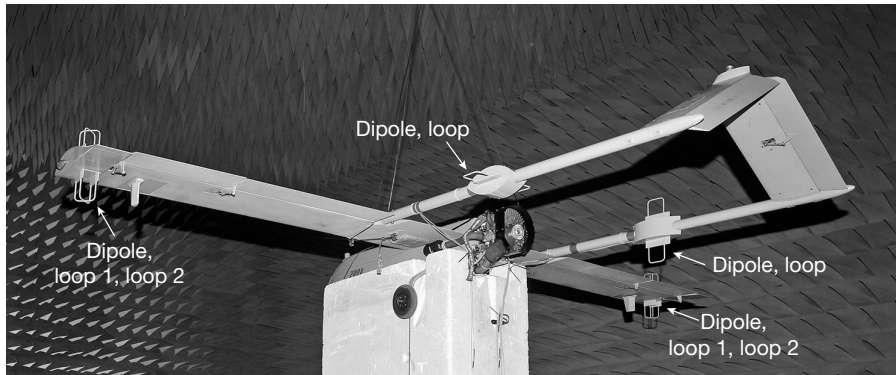


**Figure 5.2** Photograph of a sparse array of partial vector sensor antennas installed on an unmanned air vehicle.

mounted on the wing tips and they generate a dipole mode and two crossed loop antenna modes. Note that since the wings in this case are electrically conducting, a horizontal loop or dipole would be shorted out and would not be an effective receive antenna. Single loops are mounted on the tail booms and generate dipole and loop antenna modes – one of the loops is mounted horizontally and the other vertically.

### 5.2.3 Prototype 3: Full Vector Sensor with Vertical Crossed Loops, Uniform Current Loop, and a Monopole for a Nanosatellite

Examples of nanosatellite structures in the form of commercial CubeSats are depicted in the photograph shown in Figure 5.3. In this photograph two sizes of CubeSats are shown. On the left is a 10 cm x 10 cm x 30 cm version (referred to as a 3U structure), and on the right is a 10 cm x 10 cm x 10 cm (1U structure). These structures are shown in a skeletonized form where other components can be mounted. A photograph of a deployable vector sensor mechanical mockup with 3m long electrically-conducting metal tape measure loops (tip-to-tip) on a 3U CubeSat structure during preliminary ground-based mechanical testing [11, 14] is shown in Figure 5.4. In this photograph, gravity-offload structural members are included to provide support to the metal tape

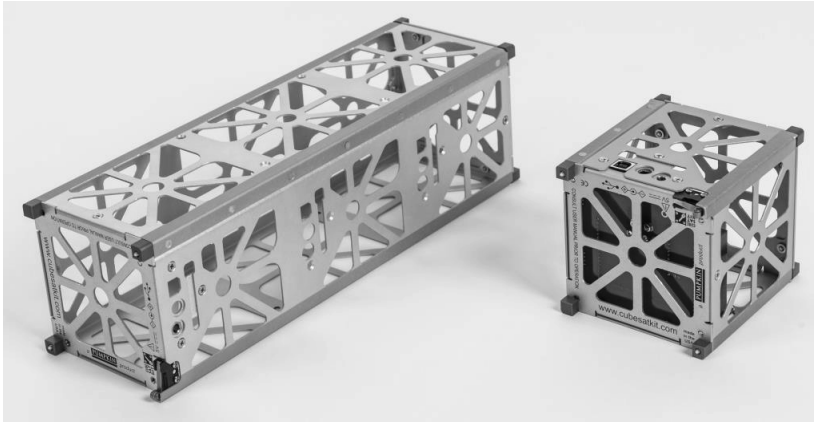


**Figure 5.3** Photograph of commercial CubeSat mechanical structures. Left: 10 cm x 10 cm x 30 cm version (3U). Right: 10 cm x 10 cm x 10 cm (1U).

loops as they deploy. The electromagnetic design and simulations of this prototype CubeSat vector sensor antenna are given in Section 5.4. The next section describes the vector sensor antenna modes.

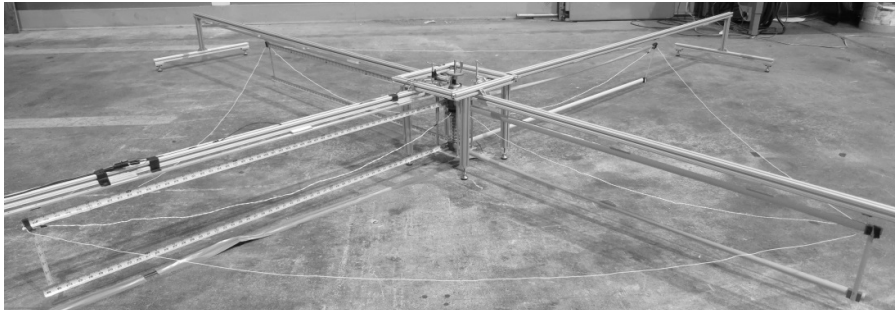


**Figure 5.4** Photograph of a vector sensor antenna deployed from a CubeSat 3U mockup during preliminary mechanical testing for a CubeSat application.

### 5.3 Vector Sensor Antenna Modes

To describe the operating modes of vector sensor antennas, consider Figure 5.5 that shows an example simplified partial vector sensor antenna. This antenna has the appearance of crossed electrically conducting loops operating in the presence of an electrically conducting ground plane. In general, a ground plane is not required, but in the case of the UAV in Figure 5.2 the wing acts as a ground plane and support structure. Additionally, the ground

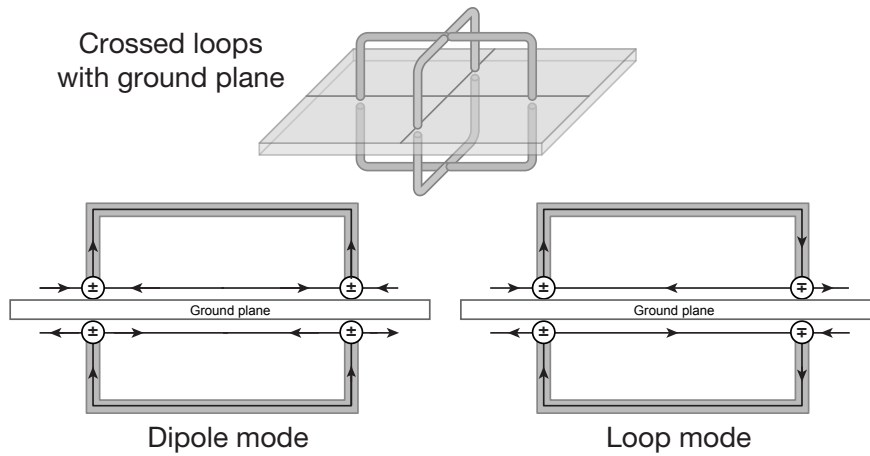


**Figure 5.5** Conceptual diagrams showing a crossed-loop vector sensor antenna on a conducting ground plane with the antenna operating in dipole and loop modes.

plane shown here will also be considered a nanosatellite structure in the next example. The antenna is assumed to be electrically small in terms of wavelength and will have a frequency independent radiation pattern for each of the operating modes.

Each physical loop has four RF ports and they are driven with a modeforming (beamforming) RF circuit that generates independent dipole and loop modes. By symmetry, the crossed loops can be electrically connected at the orthogonal intersection points in this diagram, without disturbing the two modes. That is, the two modes will not couple significantly with one another. By driving the ports in a common phase direction as shown in the lower left portion of this figure, a dipole mode is generated from the vertically flowing currents. In this dipole mode, the currents that flow on the horizontal sections of the loop and on the ground plane are out of phase and would not contribute to the far-zone radiation pattern. In the lower right diagram, the ports are now driven in a phase difference arrangement causing the electric currents to flow in a clockwise or loop fashion. Again, in this loop mode, currents flowing on the ground plane are out of phase and do not contribute to the far-zone radiation pattern.

In the case where the two crossed loops are driven in a common phase condition, the currents on the four vertical segments of the loops are in phase as depicted in Figure 5.6, which generates an effective dipole mode. When the loops are driven with a  $180^\circ$  phase difference, the loop mode is generated as

shown in Figure 5.7.

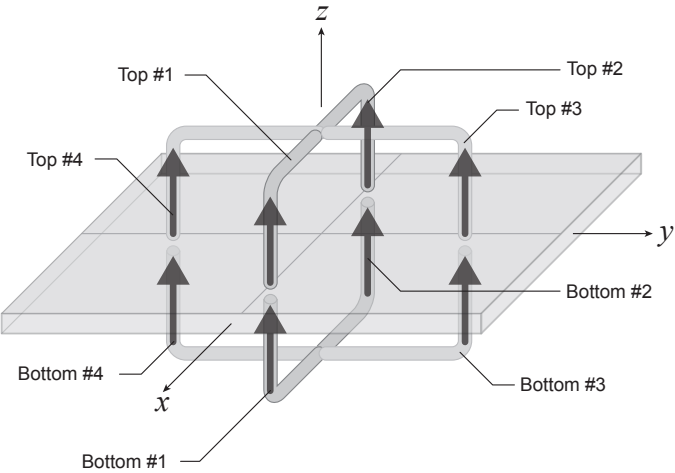


**Figure 5.6** Conceptual diagram showing a crossed-loop partial vector sensor antenna operating in the dipole mode.

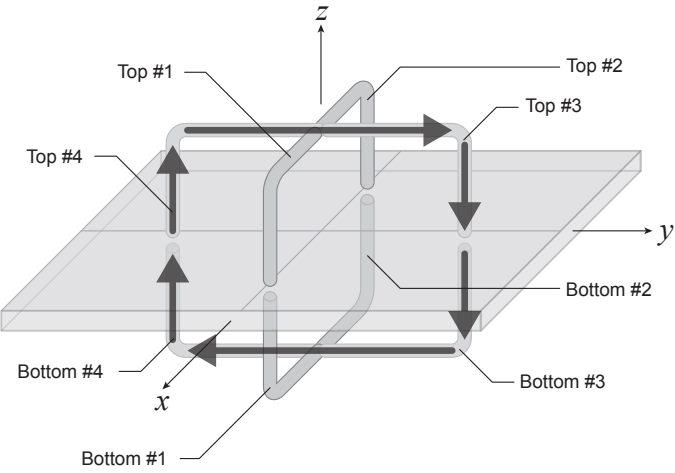


**Figure 5.7** Conceptual diagram showing a crossed-loop partial vector sensor antenna operating in the loop mode.

## 5.4 Vector Sensor Antenna Design and Simulated Radiation Patterns for a Nanosatellite Application

It is known from the literature that mapping of radio frequency galactic noise-like sources can be determined by ground based large diameter antenna array measurements for frequencies above about 25 MHz [20–23]. Due to the total electron content of the ionosphere [21], radio frequency sources radiating below about 25 MHz are partially or almost completely reflected by the ionosphere. Therefore, the electromagnetic waves from galactic radiofrequency sources are partially or almost completely blocked by the earth's ionosphere up to an altitude of about 300 km. Terrestrial radio frequency emissions are a significant source of interference for ground-based low-frequency mapping sensors. The natural radio frequency shielding provided by the ionosphere reduces terrestrial interference that would be received by a low-frequency satellite sensor orbiting above the ionosphere. Thus, mapping of galactic RF sources below 25 MHz can best be accomplished from a spacecraft above 300 km altitude. Multipolarized vector sensor antenna systems are being explored for a variety of direction finding applications [1–17] and these sensors when deployed on a nanosatellite in orbit above the ionosphere are an alternate approach to mapping galactic sources. Ideally, measurements from the vector sensor antenna elements should be dominated by external sources rather than by internal thermal noise due to electronic components such as low noise amplifiers (LNAs). HF systems operating as a beacon have been designed for CubeSats [19], and could potentially be used in calibrating an orbiting vector sensor array.

A full electromagnetic vector sensor antenna [2] characterizes the electromagnetic field at a single location in space and with a common phase center. A full vector sensor is composed of three orthogonal dipole modes and three orthogonal loop modes. These six modes allow for a complete measurement of the electromagnetic field amplitude and phase of incoming radiation. The full six-mode vector sensor antenna design here uses the following approach for a CubeSat application as shown in Figure 5.8. The axis of the CubeSat is aligned with the  $z$  axis with the radiation patterns characterized in spherical coordinates by  $\hat{\theta}$  and  $\hat{\phi}$  polarizations. King has shown that a loop antenna can also operate as a dipole [24]. Loop and dipole antenna modes are generated from crossed vertical dual mode loop elements. As shown in this diagram there are two dipole modes labeled as  $x$ -dipole (Mode 1) and  $y$ -dipole (Mode 3) that are aligned with the  $x$  and  $y$  axes, respectively. There are two loop modes labeled as  $x$ -loop (Mode 2) and  $y$ -loop (Mode 4), with the axes of the loops aligned with the  $x$  and  $y$  axes, respectively. Note that a wide bandwidth for signal to noise ratio (SNR) can



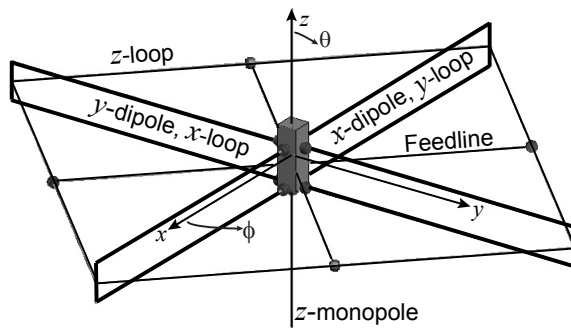


**Figure 5.8** Conceptual diagram for a full vector sensor deployed from a CubeSat structure.

be achieved for the vector sensor dipole and loop modes with active matching circuitry as discussed by Robey et al [13]. Similar active matching circuits for antennas have been described by Grubb [25], Nordholt [26], and Li [27]. The  $z$ -monopole antenna (Mode 5) is fed against the CubeSat structure and is omnidirectional with respect to the  $z$  axis. The horizontal  $z$ -loop antenna (Mode 6) is fed at four ports (by the feedlines shown) and is omnidirectional with respect to the  $z$  axis. To achieve a uniform electric current, the four ports of the horizontal loop are fed with the same positive and negative polarity with respect to rotation about the  $z$  axis. To illuminate the four ports of the horizontal loop with equal amplitude, the four feedlines are driven by a four-way power combiner.

The vector sensor antennas would be stowed for launch and then deployed on-orbit. The vector sensor antenna system described here can also be installed on a tower or launched from a balloon [13] and be used to map radio sources at frequencies above about 25 MHz where the ionospheric shielding is reduced.

The wire length of the vector sensor antenna arms is chosen in the range of 1.5m to 2m and keeps the antennas electrically small, below resonance, so that constant radiation pattern shapes are maintained over the desired frequency range. The four modes associated with the two crossed wire loop antennas and two crossed horizontal dipole antennas are generated by sum and difference modeformers. Figure 5.9 shows a diagram of a simplified circuit model to provide sum and difference outputs for a four-port loop attached to a CubeSat structure. The dipole currents are generated by the sum port of the hybrid component. Similarly, Figure 5.10 depicts the loop currents that are generated by the difference port of the hybrid component.

Radiation patterns were computed using the FEKO method of moments solver. The CubeSat body was modeled with triangular patch basis functions.

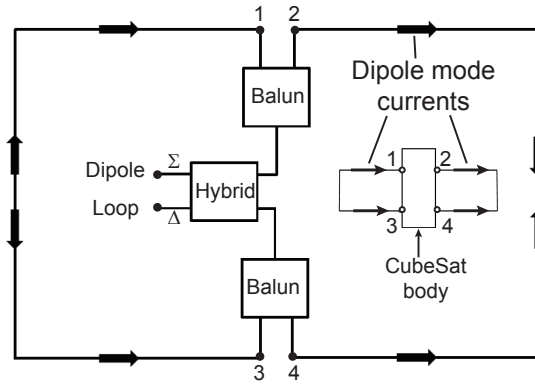


**Figure 5.9** Diagram showing a simplified circuit model to provide sum and difference outputs for a four-port loop. The dipole currents are generated by the sum port of the hybrid component.

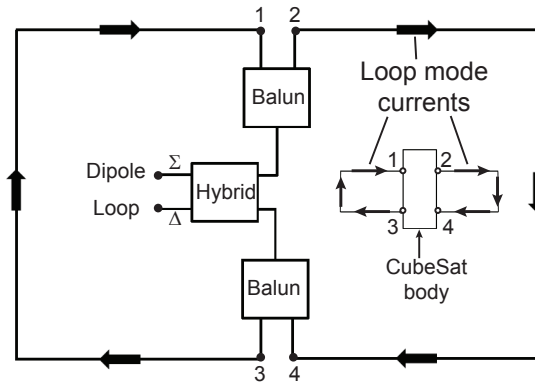


**Figure 5.10** Diagram showing a simplified circuit model to provide sum and difference outputs for a four-port loop. The loop currents are generated by the difference port of the hybrid component.

The loop and monopole antennas were modeled using triangular linear basis functions. The 10 MHz normalized radiation patterns of the six modes are shown in Figure 5.11. It is observed that the radiation patterns of Modes 1 and 4 have equivalent shapes, but they are orthogonally polarized – the Mode 1 ( $x$  dipole) relative gain pattern is  $\hat{\theta}$  polarized and the Mode 4 ( $y$  loop) is  $\hat{\phi}$  polarized. Similarly, Modes 2 and 3 have equivalent radiation pattern shapes and are orthogonally polarized. Finally, Modes 5 and 6 have the same pattern shapes and are orthogonally polarized. These six modes allow a complete characterization of the incident electromagnetic field. In the next section, the

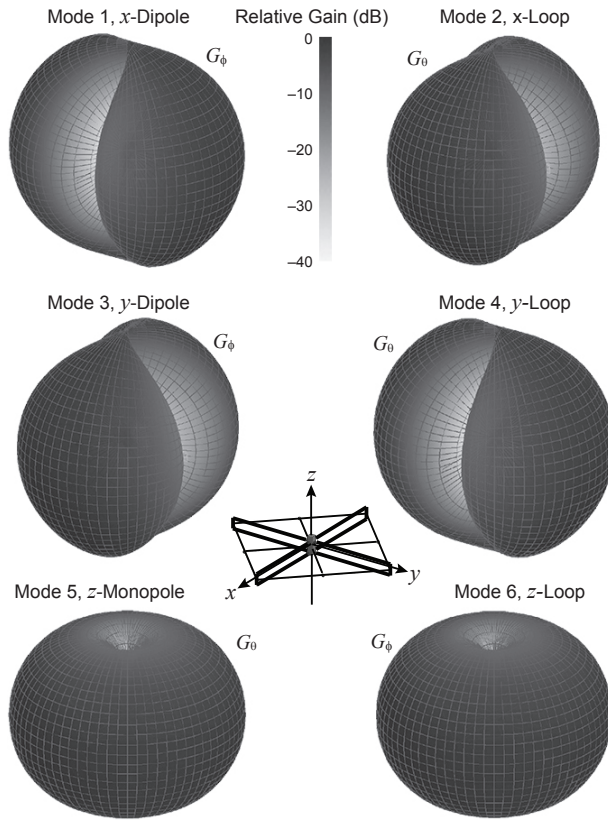


**Figure 5.11** Normalized radiation patterns for all six vector sensor modes.

radiation patterns of the six modes in closed form are used to derive the vector sensor receive voltage matrix. From this voltage matrix the covariance matrix can be computed and is used in the signal processing and mapping of incident RF fields from galactic sources [11].

## 5.5 Vector Sensor Antenna Receive Voltage Derivation

Assume that a vector sensor antenna has six receive modes consisting of  $x$ ,  $y$ , and  $z$  oriented dipoles and  $x$ ,  $y$ , and  $z$  oriented loops. The dipole and loop antennas have a common phase center that is assumed to be located at the origin of the standard spherical coordinate system. The angle  $\theta$  is measured with respect to the  $z$  axis and  $\phi$  is the angle with respect to the  $xy$  plane.

The electromagnetic fields of ideal electrically short dipole and small loop antennas can be expressed in closed form as given below.

When the electric dipole moment has only an  $x$  orientation, that is,  $\mathbf{I}_e l = \hat{x} I_e l$ , the far-zone fields are given by (refer to Equations (1.496) and (1.497))

$$\mathbf{E}_{x\text{-dipole}}^{FF}(\mathbf{r}) = \left[ -\hat{\theta} \cos \theta \cos \phi + \hat{\phi} \sin \phi \right] j k I_e l \eta \frac{e^{-jkr}}{4\pi r}. \quad (5.1)$$

$$\mathbf{H}_{x\text{-dipole}}^{FF}(\mathbf{r}) = - \left[ \hat{\theta} \sin \phi + \hat{\phi} \cos \theta \cos \phi \right] j k I_e l \frac{e^{-jkr}}{4\pi r}. \quad (5.2)$$

The loop fields are given by (refer to Equations (1.502) and (1.503))

$$\mathbf{E}_{x\text{-loop}}^{FF}(\mathbf{r}) = - \left[ \hat{\theta} \sin \phi + \hat{\phi} \cos \theta \cos \phi \right] \eta k^2 I A \frac{e^{-jkr}}{4\pi r}. \quad (5.3)$$

$$\mathbf{H}_{x\text{-loop}}^{FF}(\mathbf{r}) = \left[ \hat{\theta} \cos \theta \cos \phi - \hat{\phi} \sin \phi \right] k^2 I A \frac{e^{-jkr}}{4\pi r}. \quad (5.4)$$

When the electric dipole moment has only a  $y$  orientation, that is,  $\mathbf{I}_e l = \hat{y} I_e l$ , the far-zone fields are given by (refer to Equations (1.500) and (1.501))

$$\mathbf{E}_{y\text{-dipole}}^{FF}(\mathbf{r}) = - \left[ \hat{\theta} \cos \theta \sin \phi + \hat{\phi} \cos \phi \right] j k \eta I_e l \frac{e^{-jkr}}{4\pi r}. \quad (5.5)$$

$$\mathbf{H}_{y\text{-dipole}}^{FF}(\mathbf{r}) = \left[ \hat{\theta} \cos \phi - \hat{\phi} \cos \theta \sin \phi \right] j k I_e l \frac{e^{-jkr}}{4\pi r}. \quad (5.6)$$

The loop fields are given by (refer to Equations (1.502) and (1.503))

$$\mathbf{E}_{y\text{-loop}}^{FF}(\mathbf{r}) = \left[ \hat{\theta} \cos \phi - \hat{\phi} \cos \theta \sin \phi \right] \eta k^2 I A \frac{e^{-jkr}}{4\pi r}. \quad (5.7)$$

$$\mathbf{H}_{y\text{-loop}}^{FF}(\mathbf{r}) = \left[ \hat{\theta} \cos \theta \sin \phi + \hat{\phi} \cos \phi \right] k^2 I A \frac{e^{-jkr}}{4\pi r}. \quad (5.8)$$

When the electric dipole moment has only a  $z$  orientation, that is,  $\mathbf{I}_e l = \hat{z} I_e l$ , the far-field vector components are given by (refer to Equations (1.488) and (1.489))

$$\mathbf{E}_{z\text{-dipole}}^{FF}(\mathbf{r}) = \hat{\theta} j \omega \mu I_e l \frac{e^{-jkr}}{4\pi r} \sin \theta \quad (5.9)$$

$$\mathbf{H}_{z\text{-dipole}}^{FF}(\mathbf{r}) = \hat{\phi} I_e l j k \frac{e^{-jkr}}{4\pi r} \sin \theta. \quad (5.10)$$

The far-zone fields for the Hertzian magnetic dipole (electric current loop) oriented with the axis in the  $z$  direction, that is,  $\mathbf{m} = m\hat{\mathbf{z}}$ , where  $m = IA$ , are given by (refer to Equations (1.488) and (1.489))

$$\mathbf{E}_{z\text{-loop}}^{FF}(\mathbf{r}) = \hat{\phi} IA \omega \mu k \frac{e^{-jkr}}{4\pi r} \sin \theta. \quad (5.11)$$

$$\mathbf{H}_{z\text{-loop}}^{FF}(\mathbf{r}) = -\hat{\theta} k^2 IA \frac{e^{-jkr}}{4\pi r} \sin \theta \quad (5.12)$$

Now consider the received voltage for a plane wave impinging on a vector sensor antenna with ideal short dipole and small loop elements. Utilizing the generalized antenna vector effective height ( $\mathbf{h}$ ), which has units of meters, the induced open-circuit voltage across the terminals of an antenna is given by

$$V = \mathbf{E}_{\text{inc}} \cdot \mathbf{h}^* = \mathbf{h}^* \cdot \mathbf{E}_{\text{inc}} \quad (5.13)$$

where

$$\mathbf{h} = h \hat{\mathbf{p}}_a = \mathbf{p}_a \quad (5.14)$$

and where  $h$  is the magnitude of the vector effective height and  $\hat{\mathbf{p}}_a$  is the unit vector polarization response of the antenna. Now, from Equations (5.1), (5.5), (5.19) for the dipole modes and (5.3), (5.7), and (5.11) for the loop modes, the polarization response matrix of the vector sensor antenna array is given in terms of the  $\hat{\theta}$  (first column) and  $\hat{\phi}$  (second column) components by

$$\mathbf{p}_a = \begin{bmatrix} \cos \theta \cos \phi & -\sin \phi \\ \cos \theta \sin \phi & \cos \phi \\ -\sin \theta & 0 \\ -\sin \phi & -\cos \theta \cos \phi \\ \cos \phi & -\cos \theta \sin \phi \\ 0 & \sin \theta \end{bmatrix} \quad (5.15)$$

Note that the first three rows of the  $\mathbf{p}_a$  matrix in Equation (5.15) correspond to the  $\hat{x}$ ,  $\hat{y}$ , and  $\hat{z}$  dipole modes and the last three rows correspond to the  $\hat{x}$ ,  $\hat{y}$ , and  $\hat{z}$  loop modes.

Now from the derivation given in Chapter 1 (Equation 1.517), recall that that the incident wave electric-field unit vector  $\hat{\mathbf{e}}^{\text{inc}}$  or incident polarization unit vector  $\hat{\mathbf{p}}^{\text{inc}}$  in spherical coordinates is given by

$$\hat{\mathbf{e}}^{\text{inc}} = \hat{\mathbf{p}}^{\text{inc}} = \frac{E_{\theta}^{\text{inc}}}{|\mathbf{E}|} \hat{\theta} + \frac{E_{\phi}^{\text{inc}}}{|\mathbf{E}|} \hat{\phi} = \sin \gamma_p e^{j\delta_p} \hat{\theta} + \cos \gamma_p \hat{\phi}. \quad (5.16)$$

and observe that

$$\sin \gamma_p = \frac{E_{\theta}^{\text{inc}}}{|\mathbf{E}|} \quad (5.17)$$

$$\cos \gamma_p = \frac{E_\phi^{\text{inc}}}{|\mathbf{E}|} \quad (5.18)$$

where

$$|\mathbf{E}| = \sqrt{E_\theta^2 + E_\phi^2} \quad (5.19)$$

In the matrix form of Equation (5.16), the incident polarization unit vector is given by

$$\hat{\mathbf{p}}^{\text{inc}} = \begin{bmatrix} \sin \gamma_p e^{j\delta_p} \\ \cos \gamma_p \end{bmatrix} \quad (5.20)$$

The full vector sensor received signal voltage 6 x 1 matrix  $\mathbf{V}$  is formed by the product of the 6 x 2 matrix for the antenna polarization response  $\mathbf{p}_a$  given by Equation (5.15) and the 2 x 1 matrix for the incident field polarization  $\hat{\mathbf{p}}^{\text{inc}}$  as

$$\mathbf{V} = \hat{\mathbf{p}}_a^* \cdot \hat{\mathbf{p}}^{\text{inc}} = \begin{bmatrix} \cos \theta \cos \phi & -\sin \phi \\ \cos \theta \sin \phi & \cos \phi \\ -\sin \theta & 0 \\ -\sin \phi & -\cos \theta \cos \phi \\ \cos \phi & -\cos \theta \sin \phi \\ 0 & \sin \theta \end{bmatrix} \begin{bmatrix} \sin \gamma_p e^{j\delta_p} \\ \cos \gamma_p \end{bmatrix} \quad (5.21)$$

which is the desired result. The voltage matrix given by Equation (5.21) is expressed in a normalized form. Taking account of the incident field strength, the absolute form of the voltage matrix is used in computing a 6 x 6 covariance matrix, which is then used in mapping galactic sources as described by Knapp et al [11].

## 5.6 Summary

Vector sensor array antenna systems are used to measure multiple polarization components of an incident electromagnetic field. A few examples of vector sensor antenna prototypes have been described in this chapter. The design of a vector sensor HF antenna array that could be integrated on a small satellite has been described. Moment method simulated radiation patterns for the various vector sensor modes have been shown. A derivation of the receive voltage matrix for the vector sensor array has been given. A potential future application is for performing radio astronomy missions. The antenna technology described here could be applied to other platforms such as airborne vehicles, towers, ground vehicles, and ballon-based applications.

## References

- [1] G.F. Hatke, "Conditions for Unambiguous Source Location Using Polarization Diverse Arrays," *Proc. 27th Asilomar Conference on Signals, Systems and Computers*, 1993, pp. 1365–1369.
- [2] A. Nehorai and E. Paldi, "Vector-Sensor Array Processing for Electromagnetic Source Localization," *IEEE Trans. Signal Proc.*, vol. 42, no. 2, 1994, pp. 376–398.
- [3] S. Appadwedula and C. M. Keller, "Direction-Finding Results for a Vector Sensor Antenna on a Small UAV," *Proc. IEEE Workshop on Sensor Array and Multichannel Signal Proc.*, July 2006, pp. 74–78.
- [4] H.S. Mir, "Transfer Function Based Approaches to Array Calibration," *J. of Communications*, vol. 2, no. 3, 2007, pp. 58–63.
- [5] H. Mir and J. Sahr, "Calibration of a Polarization Diverse Array," *Int. Conf. on Acous. Speech and Sig. Proc.*, May 2006, pp. 1065–1068.
- [6] H. Mir and J. Sahr, "Passive Direction Finding Using Airborne Vector Sensors in the Presence of Manifold Perturbations," *IEEE Trans. Sig. Proc.*, vol. 55, no. 1, 2007, pp. 156–164.
- [7] A.J. Fenn and P.T. Hurst, *Ultrawideband Phased Array Antenna Technology for Sensing and Communications Systems*, MIT Lincoln Laboratory Book Series, Cambridge, MA: The MIT Press, 2015, pp. 255–273.
- [8] R.T. Compton, "The Tripole Antenna: An Adaptive Array with Full Polarization Flexibility," *IEEE Trans. Antennas and Propagation*, vol. 29, no. 11, 1981, pp. 944–952.
- [9] A.J. Fenn, F.C. Robey, P.T. Hurst, M.J. Silver, "Multipolarized Vector Sensor Array Antenna System for Radio Astronomy Applications," Provisional Application number US62243343, Filing date: Oct. 19, 2015.
- [10] A.J. Fenn, B. Zhang, P.T. Hurst, K.E. Kolodziej, L.L. Retherford, C.D. Austin, "Multipolarized Vector Sensor Array Antenna System for Search and Rescue Applications," Application number PCT/US2016/027269, Publication date, Oct 20, 2016.
- [11] M. Knapp, F. Robey, R. Volz, F. Lind, A. Fenn, A. Morris, M. Silver, S. Klein, and S. Seager, "Vector Antenna and Maximum Likelihood Imaging for Radio Astronomy," *2016 IEEE Aerospace Conference*, Big Sky, Montana, 5-12 March 2016, pp. 1–17.
- [12] M. Knapp, F. Robey, R. Volz, Frank Lind, A. Fenn, A. Morris, M. Silver, S. Klein, and S. Seager, "Vector Antenna and Maximum Likelihood Imaging for Radio Astronomy," *IEEE Aerospace Conference*, 2016, pp. 1-17.
- [13] F. Robey C., M. Knapp, A.J. Fenn, M. Silver, K. Johnson, F.J. Lind, R. Volz, S. Seager, and F. Neylon-Azad, "High Frequency (HF) Radio Astronomy from a Small Satellite," *Small Sat Conference*, 2016.
- [14] M. Knapp, R. Volz, Frank D. F. Lind C. Robey, A. Fenn, K. Johnson, M. Silver, A. Morris, and S. Klein, "HF Vector Sensor for Radio Astronomy: Ground Testing Results," *AIAA SPACE 2016*, p. 5498.
- [15] R. Volz, M. Knapp, F. Lind, F. Robey, "Covariance Estimation in Terms of Stokes Parameters with Application to Vector Sensor Imaging," *Proc. 51st Asilomar*

*Conference on Signals and Systems*, Nov. 2016.

- [16] M. Knapp, D. Gary, M. Hecht, F. Lind, C. Lonsdale, F. Robey, "HERO: A Spacebased Low Frequency Interferometric Observatory for Heliophysics Enabled by Novel Vector Sensor Technology" *8th International Workshop on Planetary, Solar, and Heliospheric Radio Emissions (PRE8)*, November 2016
- [17] M. Knapp, F. Robey, R. Volz, Frank Lind, A. Fenn, A. Morris, M. Silver, S. Klein, and S. Seager. "HeRO: Heliophysics Radio Observer." *Science at Low Frequencies*, Dec. 2016.
- [18] W.W. Lee, M. Parent, and G. San Antonio, "High Frequency Vector Sensor Design and Testing," *NRL Review*, 2013, pp. 154–156.
- [19] R. Lehmensiek, R. R. van Zyl and D. F. Visser, "The Design of an HF Antenna on a 1U CubeSat," *Africon* 9–12 Sept. 2013, pp. 1–4.
- [20] A.S. Cohen, W.M. Lane, W.D. Cotton, N.E. Kassim, T.J. W. Lazio, R.A. Perley, J.J. Condon, and W.C. Erickson, "The VLA Low-Frequency Sky Survey," *The Astronomical J.*, vol. 134, Sept. 2007, pp. 1245–1262.
- [21] N.E. Kassim, T. Joseph W. Lazio, W.C. Erickson, R.A. Perley, W.D. Cotton, E.W. Greisen, A.S. Cohen, B. Hicks, H.R. Schmitt, and D. Katz, "The 74 MHz System on the Very Large Array," *The Astrophysical J. Supplement Series*, vol. 172, Oct., 2007, pp. 686–719.
- [22] W.M. Lane, W.D. Cotton, S. van Velzen, T.E. Clarke, N.E. Kassim, J.F. Helmboldt, T.J.W. Lazio, and A.S. Cohen, "The Very Large Array Low-frequency Sky Survey Redux (VLSSr)," *Monthly Notices of the Royal Astronomical Soc.*, 4 April 2014, Accessed online: <http://arxiv.org/pdf/1404.0694v1.pdf>
- [23] S. Jester and H. Falcke, "Science with a Lunar Low-Frequency Array: From the Dark Ages of the Universe to Nearby Exoplanets," *New Astronomy Reviews*, vol. 53, 2009, pp. 1–26.
- [24] R. King, "The Rectangular Loop Antenna as a Dipole," *IRE Trans. on Antennas and Propagation*, vol. 7, no. 1, Jan. 1959, pp. 53–61.
- [25] R.N. Grubb, R. Livingston, T.W. Bullett, "A New General Purpose High Performance HF Radar," *Proc. 2008 URSI General Assy Comm. G*, <http://www.ursi.org/proceedings/procGA08/papers/GHp4.pdf>, [Accessed: 2 March 2017], pp. 1–4.
- [26] E.H. Nordholt and F. Van Willigen. "A New Approach to Active Antenna Design," *IEEE Trans. on Antennas and Propagation*, vol. AP-28, no. 6, Nov. 1980, pp. 904–909.
- [27] W. Li, R. Chen, N. Zhai, S. Li, R. Mittra, "Wideband Matching of an Electrically Small Antenna Using a Negative Impedance Converter Technique," *Proc. 2012 IEEE Int. Symp. on Antennas and Propagation*, 2012, pp. 1–2.